JGR Space Physics

RESEARCH ARTICLE
10.1029/2024JA032821

†Deceased

Key Points:

- Ions and electrons accelerated by 10–50 keV near the magnetotail reconnection can reach the inner magnetosphere
- A partial ring current is formed during the simulation, with highest energy flux between midnight and dusk
- The ion and electron energy fluxes are mostly kinetic in the reconnection region but change to enthalpy flux earthward

Supporting Information:

Supporting Information may be found in the online version of this article.

Correspondence to:

L. Rusaitis,
liutauras.rusaitis@nasa.gov

Citation:

Rusaitis, L., El-Alaoui, M., Walker, R. J., Lapenta, G., & Schriver, D. (2024). A multi-scale particle-in-cell simulation of plasma dynamics from magnetotail reconnection to the inner magnetosphere. *Journal of Geophysical Research: Space Physics*, *129*, e2024JA032821. https://doi.org/10.1029/2024JA032821

Received 26 APR 2024
Accepted 8 SEP 2024

Author Contributions:

Conceptualization: L. Rusaitis, M. El-Alaoui
Data curation: L. Rusaitis
Formal analysis: L. Rusaitis, R. J. Walker
Funding acquisition: M. El-Alaoui
Investigation: L. Rusaitis, M. El-Alaoui, R. J. Walker, G. Lapenta, D. Schriver
Methodology: L. Rusaitis, M. El-Alaoui, R. J. Walker
Project administration: M. El-Alaoui
Resources: L. Rusaitis, G. Lapenta
Software: L. Rusaitis, G. Lapenta
Supervision: M. El-Alaoui, R. J. Walker
Validation: L. Rusaitis
Visualization: L. Rusaitis
Writing – original draft: L. Rusaitis
Writing – review & editing: L. Rusaitis, M. El-Alaoui, R. J. Walker, G. Lapenta, D. Schriver

A Multi-Scale Particle-In-Cell Simulation of Plasma Dynamics From Magnetotail Reconnection to the Inner Magnetosphere

L. Rusaitis[1,2], M. El-Alaoui[1,2†], R. J. Walker[3], G. Lapenta[†], and D. Schriver[1,2,4]

[1]Community Coordinated Modeling Center, NASA Goddard Space Flight Center, Greenbelt, MD, USA, [2]Department of Physics, CUA, Washington, DC, USA, [3]Department of Earth, Planetary, and Space Sciences, University of California, Los Angeles, CA, USA, [4]Department of Physics and Astronomy, University of California, Los Angeles, CA, USA

Abstract During magnetospheric substorms, plasma from magnetic reconnection in the magnetotail is thought to reach the inner magnetosphere and form a partial ring current. We simulate this process using a fully kinetic 3D particle-in-cell (PIC) numerical code along with a global magnetohydrodynamics (MHD) model. The PIC simulation extends from the solar wind outside the bow shock to beyond the reconnection region in the tail, while the MHD code extends much further and is run for nominal solar wind parameters and a southward interplanetary magnetic field. By the end of the PIC calculation, ions and electrons from the tail reconnection reach the inner magnetosphere and form a partial ring current and diamagnetic current. The primary source of particles to the inner magnetosphere is bursty bulk flows (BBFs) that originate from a complex pattern of reconnection in the near-Earth magnetotail at $x_{\mathrm{GSM}} = -18R_{\mathrm{E}}$ to $-30R_{\mathrm{E}}$. Most ion acceleration occurs in this region, gaining from 10 to 50 keV as they traverse the sites of active reconnection. Electrons jet away from the reconnection region much faster than the ions, setting up an ambipolar electric field allowing the ions to catch up after approximately 10 ion inertial lengths. The initial energy flux in the BBFs is mainly kinetic energy flux from the ions, but as they move earthward, the energy flux changes to enthalpy flux at the ring current. The power delivered from the tail reconnection in the simulation to the inner magnetosphere is $>2 \times 10^{11}$ W, which is consistent with observations.

Plain Language Summary During intervals of increased solar activity, the magnetic field in Earth's stretched night-side tail undergoes intense reconfiguration that can energize particles. This process is called magnetic reconnection. Ions and electrons from reconnection can reach the inner magnetosphere. In this paper, we simulate this process using a novel model that includes Earth's global magnetic field configuration and self-consistently models particle physics for both electrons and ions. We find that the particles are accelerated significantly near the sites of magnetic field reconfiguration with ions gaining 10 s of keV energy. As they propagate earthward, they end up contributing energetically to the formation of a ring current system partially encircling Earth.

1. Introduction

During geomagnetically active periods, particles from the magnetotail are thought to enter the inner magnetosphere, intensifying a partial ring current located roughly at 4–7 R_{E}. It is strongest from midnight to dusk near the equator, and its total current can reach three times that of the inner symmetric ring current (Le et al., 2004). The trapped ring-current particles perform a complex particle drift, acceleration, and loss in time-varying electromagnetic fields, significantly affecting the near-Earth environment. The ions are detected with energies of 10–200 keV and electrons of 10 keV up to MeV (Frank, 1967; Smith & Hoffman, 1973; Williams, 1981). The main focus of this work is the intensification of this partial ring current by particles accelerated in the magnetotail and transported earthward through fast-flow channels.

The fast flows of plasma from the magnetotail toward the inner magnetosphere frequently are in the form of narrow channels called bursty bulk flows (BBFs) (Angelopoulos et al., 1992, 1994). The properties of BBFs have been extensively studied since their discovery; see L. Q. Zhang et al. (2016) for a review of the properties of BBFs and their dependence on magnetospheric activity. They flow earthward at hundreds of km/s and are 1 R_{E} or 2 R_{E} wide in the east–west direction. At their earthward edge, the magnetic field increases primarily in the northward direction forming dipolarization fronts (e.g., Runov et al., 2011). Recently a series of investigations have used

Magnetosphere Multiscale (MMS) and Van Allen Probes observations to investigate BBFs between the tail and the outer radiation belts in the inner magnetosphere (e.g., Ergun et al., 2022; Turner et al., 2021, and references therein). They found that energetic particles (>100 keV) associated with the BBF can penetrate deeply into the inner magnetosphere (Ergun et al., 2022) and suggest that turbulence generated in the earthward motion of the BBF can accelerate the particles. Angelopoulos et al. (1994) estimated the total power to the ring current region to be $\sim 3 \times 10^{11}$ W with an individual BBF providing $\sim 2.7 \times 10^{10}$ W.

Sandhu et al. (2018) used Van Allen Probe spacecraft data to investigate the relationship between the ring current and magnetospheric substorms. They found that the ring current energy is higher in the expansion phase than in the substorm growth phase and that the energy increase persists into the recovery phase. The injections of 50–660 keV ions in the dusk sector were followed by the loss of energetic protons in the afternoon sector, with the particle loss likely due to wave-particle interactions. Overall, they found that the average energy input to the ring current from a substorm was $\sim 0.9 \times 10^{15}$J.

Understanding the dynamics of the inner magnetosphere is challenging because it is highly dependent on the dynamics of the outer magnetotail plasma sheet $(x_{\mathrm{GSM}} < -20R_{\mathrm{E}})$. The characteristic scales in the two regions vary greatly so that numerical simulations historically have tended to focus on one region or the other. Magnetohydrodynamic (MHD) models have long been the workhorse of global magnetospheric modeling. Global MHD results show the importance of modeling the entire solar wind and magnetosphere interaction since the actual state of the magnetosphere is not a simple superposition of idealized states. The MHD models provide the large-scale configuration of the outer magnetosphere and include tail reconnection, fast earthward flows and dipolarizations (El-Alaoui et al., 2013; Wiltberger et al., 2015) (See McPherron, El-Alaoui, Walker, Nishimura, & Weygand et al., 2020, McPherron, El-Alaoui, Walker, & Richard et al., 2020 for a recent discussion of flow from the tail to the inner magnetosphere in both observations and MHD models). Because of the abundance of energetic particles in the magnetosphere, MHD models, which do not include kinetic particle physics, are not appropriate by themselves in describing the inner magnetospheric region, and particularly the ring current.

To improve the MHD models, they have been combined with models of the inner magnetosphere. These include particle drift-loss models of the inner magnetosphere particle dynamics. Two of these are the Comprehensive Ring Current Model (CRCM) and the Ring Current-Atmosphere Interaction Model (RAM) (Jordanova et al., 1997; Liemohn et al., 1999). The most general inner magnetosphere model is the Rice Convection Model (RCM) (Harel et al., 1981; Toffoletto et al., 2004; Yang et al., 2015, 2019). Yang et al. (2015) used the equilibrium version of the RCM (RCM-E) to argue that BBFs in the form of “bubbles” (regions in which the specific entropy $pV^{5/3}$ where p is the plasma pressure and V is the flux tube volume decreases) are a major source of storm time plasma injections. Using a different approach, Sorathia et al. (2021) used the GAMERA MHD simulation and test particle calculations in the MHD fields to evaluate the energetics of ring current particles.

The University of Michigan BATSRUS model has been coupled with several ionosphere and inner magnetosphere models by using their Space Weather Modeling Framework (SWMF) (De Zeeuw et al., 2004; Glocer et al., 2013; Zaharia et al., 2010; J. Zhang et al., 2007) including RCM, CRCM and RAM. The Lyon, Fedder and Mobarry (LFM) model (Lyon et al., 2004) has been coupled with the MIX thermosphere-ionosphere model (Merkin & Lyon, 2010) and the RCM (Pembroke et al., 2012). The Global Geosphere Circulation Model (GGCM) (Raeder et al., 2008) has been combined with an ionosphere-thermosphere model (CTIM) (Cramer et al., 2017; T. Fuller-Rowell et al., 1996) and the RCM (Cramer et al., 2017). All three models provide two-way coupling. These models can simulate the overall solar wind, magnetosphere, and ionosphere interaction over long periods of time. But they do not contain the higher order moments necessary to fully model plasma kinetic particle physics. Recently, Shi et al. (2023) used a global hybrid simulation (Lin et al., 2014) called ANGIE3D to investigate the acceleration of particles in BBF from tail reconnection. The hybrid model simulates the solar wind and magnetosphere interaction by using fully kinetic ions coupled with electrons modeled as a massless fluid. Shi et al. (2023) coupled the hybrid model with particle trajectory calculations to investigate particle acceleration. They found that earthward moving particles are accelerated by the fast flows and that the particles can gain up to 50 keV by multiple interactions with the fast flows.

The significance of BBFs as a source of particles for the inner magnetosphere and the physics of their particle acceleration remain unanswered questions (Turner et al., 2021). To address these outstanding issues, we have developed a fully self-consistent PIC simulation code coupled with a global MHD simulation code to model particle dynamics from the tail reconnection region to the inner magnetosphere. This approach enables us to address kinetic particle acceleration mechanisms operating in the outer and inner magnetosphere. It includes physics not contained in the MHD/particle-tracing or hybrid-based approaches and as such augments them.

In this paper, we investigate the earthward penetration of flow channels and dipolarization fronts to the partial ring current region following magnetic reconnection in the magnetotail. In Section 2, we present a detailed discussion of the application of the implicit multi-scale iPic3D simulation model (Markidis et al., 2010) to the magnetotail region and how we have extended it to include the inner magnetosphere. Section 3.1 contains the first results from this model and shows the inward propagation of the BBFs, and formation of the partial ring current with emphasis on the flow of energy from reconnection to the inner magnetosphere and the resulting acceleration of the plasma. In Section 3.2, we present a study of 10,000 randomly selected ions and discuss their acceleration. We discuss the dynamics of the coupled reconnection, BBFs and inner magnetosphere system and present comments on future investigations that can examine in detail the electron and ion acceleration mechanisms in Section 4 and in Section 5 we summarize the results.

2. Methodology

We use a multi-scale approach based on a combination of a global MHD simulation and the ECSIM particle-in-cell code. The overall approach is the same as described in Walker et al. (2019) in which we first run a global MHD simulation to model the overall configuration of the magnetosphere and use it to drive the large-scale PIC simulation of the outer-inner magnetospheric region.

2.1. The MHD Simulation

Our global MHD simulation solves the single fluid resistive MHD equations by using plasma and IMF input from solar wind monitoring spacecraft (El-Alaoui, 2001; Raeder et al., 1995, 1998). The code uses a predictor corrector time-centered approach and is accurate to second order. Fourth order fluxes are hybridized with first-order fluxes. In regions of the magnetosphere where parameters change smoothly diffusion is very small. Since our high-order hybrid scheme with increased resolution reduces numerical dissipation, we add a resistive term in Ohm's law, given by $\mathbf{E} = -\mathbf{v} \times \mathbf{B} + \eta \mathbf{j}$ where $\mathbf{v}$ is the velocity, $\mathbf{B}$ the magnetic field, $\mathbf{j}$ is the current density and $\eta = aj^2$. The constant a is determined empirically.

For the MHD simulation used in this study, the dimensions of the simulation box are 20 R_E in the sunward direction, 300 R_E along the tail, and $-55.1R_E < y_{GSM}/z_{GSM} < 55.1R_E$ in the transverse directions. The MHD model grid is a stretched Cartesian computational grid with greater grid density in the plasma sheet region ($500 \times 360 \times 360$ grid points). The finest grid spacing is 0.12 R_E. With such a large simulation domain, all flows at the external boundaries are in the super-magnetosonic regime, which prevents information from propagating back from the boundaries and affecting physical processes in the simulations. Here, we impose a simple solar wind configuration at the inflow boundary with $B_z = -8$ nT, $v_x = -530$ km/s, $n = 6$ cm^{-3}, and thermal pressure $P = 16$ pPa, where B_z is the north–south component of the magnetic field in GSM coordinates, v_x is the velocity component along the x-axis and n is the number density.

The ionospheric part of the model includes three sources of ionospheric conductance: solar extreme ultraviolet ratdiation (EUV), diffuse auroral precipitation and discrete auroral precipitation (El-Alaoui & Lapenta, et al., 2023; El-Alaoui & Walker, et al., 2023). We model solar EUV ionization by using the empirical model of Moen and Brekke (1993). The diffuse auroral precipitation model assumes the strong pitch-angle scattering limit at the inner boundary (2.25 R_E) of the MHD simulation (Kennel & Petschek, 1966). Based on these sources, we use the formalism of Robinson et al. (1987) to calculate the ionospheric conductances.

During the simulations, we map the magnetospheric field-aligned currents $\left(j_{\parallel}\right)$ from the inner boundary of the simulation along tilted dipolar field lines into the ionosphere (1 R_E). There we solve the ionospheric current conservation equation $\nabla\left(\overset{\leftrightarrow}{\Sigma} \cdot \nabla\phi\right) = -j_{\parallel} \sin\theta$ for the ionospheric potential ϕ where $\overset{\leftrightarrow}{\Sigma}$ is the conductance tensor and θ is the inclination angle of the field line. We then map $-\nabla\phi$ back along the field lines to the inner boundary of the simulation and use $\mathbf{v} = -\nabla\phi \times \mathbf{B}/B^2$ to set the boundary condition on the magnetospheric flow. A detailed description of the application of the ionospheric model to the MHD calculation can be found in Raeder et al. (1998).

2.2. The PIC Simulation

The PIC simulation is based on the energy conserving version of the iPic3D simulation code ECSIM (Lapenta, 2017). When reconnection is already active, we select a region of interest encompassing the entire outflow jet and launch a fully kinetic PIC simulation that can study with accuracy the electron and ion motion and directly resolve particle dynamics. Most importantly, the use of the PIC approach allows us to introduce kinetic particle physics of reconnection not included in the MHD state.

The iPic3D code (Markidis et al., 2010) solves the particle equations of motion for electrons and ions and uses the full set of Maxwell's equations, discretized by using a second-order formulation based on the electric field. The field equations are solved for the electric field ($\mathbf{E}$) while the magnetic field ($\mathbf{B}$) is then computed from Faraday's law. In the most recent iPic3D implementation, the implicit moment method is replaced by the semi-implicit Energy Conserving (ECSIM) method based on the coupling of particles and fields using a mass matrix that ensures exact energy conservation (Lapenta, 2017). The conservation of charge and the enforcement of Gauss's theorem are imposed by using the method developed by Chen and Tóth (2019).

We start the PIC simulation by using a state from the MHD simulation after reconnection has already started. The MHD simulation sets both the initial and boundary conditions for the PIC simulation. We use the MHD density initially and set the initial electron and ion velocities to $\mathbf{v}_e = \mathbf{v}_{\mathrm{MHD}} + m_i\,\mathbf{j}_{\mathrm{MHD}}/(\rho_{\mathrm{MHD}} q_e)$ and $\mathbf{v}_i = \mathbf{v}_{\mathrm{MHD}} + m_e\,\mathbf{j}_{\mathrm{MHD}}/(\rho_{\mathrm{MHD}} q_i)$ where $\mathbf{v}_{\mathrm{MHD}}$ is the velocity from the MHD simulation, $\mathbf{j}_{\mathrm{MHD}}$ is the current density from the MHD simulation, $m_{i,e}$ are the ion and electron masses, ρ_{MHD} is mass density from the MHD simulations, and $q_{i,e}$ are the ion and electron charges.

MHD does not define a PIC state so we must assume an initial ion to electron temperature ratio. For this calculation we assume that $T_i/T_e = 5$, where T_i is the ion temperature and T_e is the electron temperature, based on the observed plasma sheet temperature ratio (Baumjohann & Paschmann, 1989). Note that this is just the initial temperature ratio, and the physical temperature ratio will evolve during the simulation. The ion to electron mass ratio is $m_i/m_e = 256$ with ions as the base mass and electrons more massive than in reality. After a short transient, the electrons become decoupled from the ions and produce the typical signature of kinetic reconnection, forming much faster jets that carry substantial energy. The details of the approach to load the simulation are described in Walker et al. (2019).

We use two types of boundary conditions, semi-open and driven by MHD. The particles in the boundary layer are replaced at every time step with a new population based on the reference state provided by the MHD run. The MHD-driven boundary conditions are identical to the semi-open boundary conditions for the particles, but not for the fields. The fields are imposed from the MHD state. The code smoothly transitions the fields from the internal values from the PIC calculation to the imposed values from the MHD simulation.

The PIC method has limited ability to resolve the particle energy distribution. Most PIC methods generate a drifting Maxwellian distribution by using particles of equal weight. In this approach, very few particles are generated in the tail at high speed and the vast majority have speeds close to the drift speed. To remove this limitation, we use two species each for electrons and ions. One species is the core bulk population of thermal particles, and the second species, with reduced statistical weight, represents a power law energy tail. Most importantly, the smaller weight particles contribute to the overall energy budget of the simulation. This method preserves energy conservation and the energy needed to accelerate the particles from the electromagnetic fields. The details of the method can be found in Lapenta et al. (2020).

The PIC simulation box has $460 \times 320 \times 130$ cells corresponding to the x_{GSM}, y_{GSM} and z_{GSM} directions. The box extends from $13R_{\mathrm{E}} \geq x_{\mathrm{GSM}} \geq -33R_{\mathrm{E}}$, $16R_{\mathrm{E}} \geq y_{\mathrm{GSM}} \geq -16R_{\mathrm{E}}$, $6.5R_{\mathrm{E}} \geq z_{\mathrm{GSM}} \geq -6.5R_{\mathrm{E}}$. This is large enough to include the bow shock and magnetopause on the dayside and the reconnection in the tail (Figure 1). The study uses 125 particles per cell and a time step $\omega_{\mathrm{pi}}\Delta t = 0.1$, where ω_{pi} is the ion plasma frequency. We assumed 184 d_{i} in the x-direction, 128 d_{i} in the y-direction and 52 d_{i} in the z-direction, where d_{i} is the ion inertial length. The reference ion inertial length in the magnetotail is $d_{\mathrm{i}} = 455$ km (assuming a reference density of $n = 0.25$ cm^{-3}). For these parameters, one Earth radius will correspond to 14 d_{i}. A simulation of this size including full electron dynamics requires too much computing time to be practical. Therefore, we rescale the radius of Earth with respect to an ion inertial length by a factor of 3.5. In essence, we shrink Earth by a factor of 3.5. This rescaling leaves a very large separation between the macroscales and microscales (Lapenta et al., 2020). This might appear to be a limitation of this approach, but previous papers (Tóth et al., 2017) have shown that provided the scales remain well separated, the physics is qualitatively correct, if not quantitatively precise.

The initial MHD state used in the PIC simulation is shown in Figure 1. All three panels give the values at cycle 1 ($T = 0$) from the PIC simulation. The magnetic field B_z has been plotted in the top panel. This provides a high-level view of the magnetic field near the equator. The transition (black) from red (positive B_z) to blue (negative B_z) indicates the near-Earth neutral line. Superimposed on B_z are current density streamlines in the equatorial plane. The current density in the inner magnetosphere is much larger than that in the magnetotail reaching 20 nA/m^2. However, the pattern is essentially random since there is no ring current in the MHD model. Earthward of the reconnection B_z increases, indicating dipolarization fronts. There are three dipolarizations located at about $x_{\mathrm{GSM}} \sim -18R_{\mathrm{E}}$. One region is located at about midnight, and the other two are on the dawn $\left(y_{\mathrm{GSM}} < 0\right)$ and dusk sides of the central one.

Ion flows in the x_{GSM} direction (middle panel of Figure 1) are both earthward and tailward from the reconnection site. The ion flows confirm that reconnection occurs along an irregular line that extends across the tail at an average distance of about $x_{\mathrm{GSM}} \sim -26R_{\mathrm{E}}$ and that there are several sites of active reconnection. For southward IMF, the exact pattern of reconnection in the MHD simulation is determined primarily by the ionospheric conductance model (El-Alaoui & Lapenta, et al., 2023; El-Alaoui & Walker, et al., 2023), resulting in reconnection regions that are not symmetric with respect to midnight even though IMF B_z was purely southward. Note that there are flow channels (BBF-like) structures earthward of the regions of widespread flows. The flows on either side of the BBF show vortical patterns suggesting turbulence. We have plotted a component of the pressure tensor perpendicular to the magnetic field (mostly in the $\hat{\phi}$ direction) in the bottom panel of Figure 1. The current density vectors from the top panel have been superimposed on the color pressure contours. There is an enhancement of the pressure near the inner boundary of the simulation. As will be discussed later, this pressure is lower than found in the PIC simulation. From this start, we ran the simulation for 202,500 cycles or 1 m 47 s. In the rest of this paper, we will use the elapsed time.

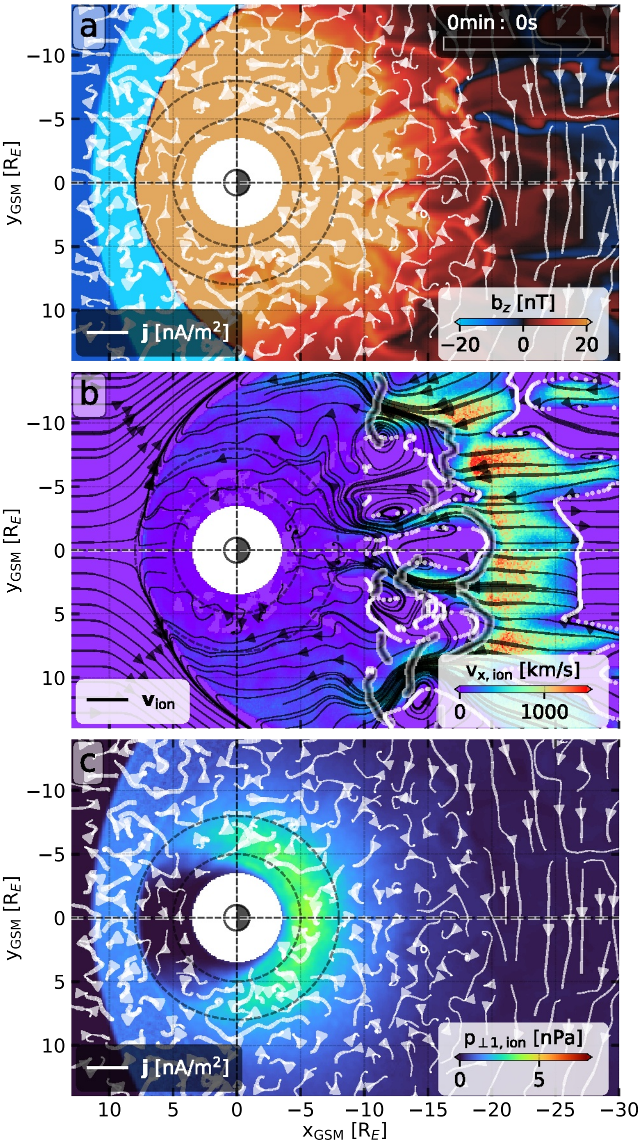

Figure 1. The top panel shows a near-equatorial ($z_{\mathrm{GSM}} = -0.05R_{\mathrm{E}}$) cut of the B_z-component of the magnetic field (color coded) and current density streamlines. The middle panel shows the ion flows in the x-direction (color coded) and flow streamlines. The lower panel illustrates one component of the perpendicular ion thermal pressure (color coded) with the current density streamlines. The thick black lines in the middle panel show the regions of dipolarization ($\Delta B_z > 2$ nT), and the white dots show flow reversals in v_x.

All simulations have limitations. It is important to understand them when interpreting the results. In Figure 2, we have plotted the number density in the top row on a logarithmic scale, the number of simulation cells per electron inertial length in the center and the number of cells per ion inertial length in the bottom row for three times in the simulation - the beginning, 53 s, and 1 m 47 s. As we will see below, the places with reconnection have very low density, typically close to 10^{-2} cm^{-3}. The PIC simulation initially does not resolve either the electron or ion inertial lengths very well (left panels). However, after the PIC state has formed the ions are much better resolved near the reconnection region and along the BBFs where the density of the particles is lower. In some places, for instance near the tail boundary, the density is $<10^{-2}$ cm^{-3}, resulting in unrealistically large magnetic fields. This does not appear to impact the rest of the simulation domain.

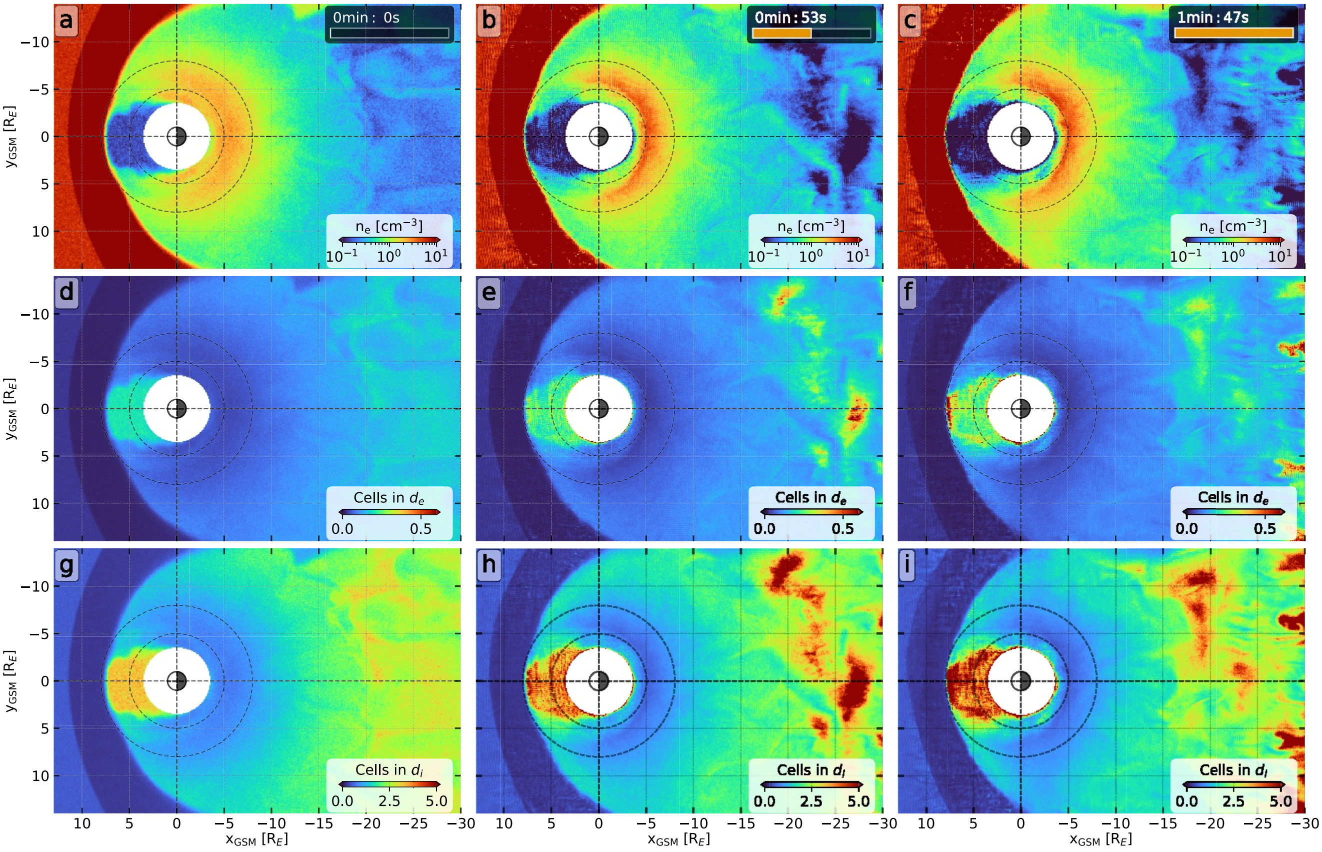

Figure 2. The top row shows the electron number density on a logarithmic scale at three different times in the PIC simulation: the first cycle is based on the MHD simulation; the second is at 53 s and the third at 1 m 47 s. The middle row shows the number of cells per electron inertial length. The bottom row shows the number of cells per ion inertial length.

3. Results

3.1. Overview of the Simulation

Figure 3 (top panel) shows the B_z component and current density streamlines at 53 s (left) and at 1 m 47 s into the PIC simulation. We have applied a Gaussian smoothing algorithm with a standard deviation of two to remove noise and highlight the ring current. The smoothing was applied to the current density and hence the velocities. Density and B_z are unsmoothed. The middle panels of Figure 3 show the x_{GSM} component of the ion velocity and velocity vectors in the same format, while the bottom panel has one perpendicular component of the ion thermal pressure and the current density vectors. These values are well after a PIC state has been established throughout the simulation box. The PIC state is characterized by particle motion not found in the MHD calculation and was present after a few seconds. The reconnection region is located with an extent $-30R_{\mathrm{E}} < x_{\mathrm{GSM}} < -18R_{\mathrm{E}}$. As noted above, there are several sites of active reconnection. At both 53 s and 1 m 47 s, the perpendicular current pattern in the magnetotail is mostly from dawn to dusk. It becomes much more complex near the reconnection sites. The smoothed current pattern in the inner magnetosphere at 53 s shows that a ring current flowing clockwise is forming between $-6R_{\mathrm{E}}$ and $-10R_{\mathrm{E}}$. The partial ring current at 53 s results mostly from the drift motion of particles loaded into the simulation. At both times, the current direction changes from clockwise to counterclockwise nearer Earth. In the bottom panels, this current reversal is in a region of enhanced thermal pressure and indicates a diamagnetic current. This can be seen more clearly in Figure 4 where we have enlarged the region in the inner magnetosphere at 1 m 47 s and show current density streamlines. The counterclockwise current is in the high-pressure region nearest Earth. The clockwise partial ring current is tailward of the diamagnetic current.

At 53 s in Figure 3 (middle), the flow reverses direction in the reconnection regions. The reconnection is not uniform across the tail. This contributes to a complex flow pattern in the tail. The ion flow velocities away from

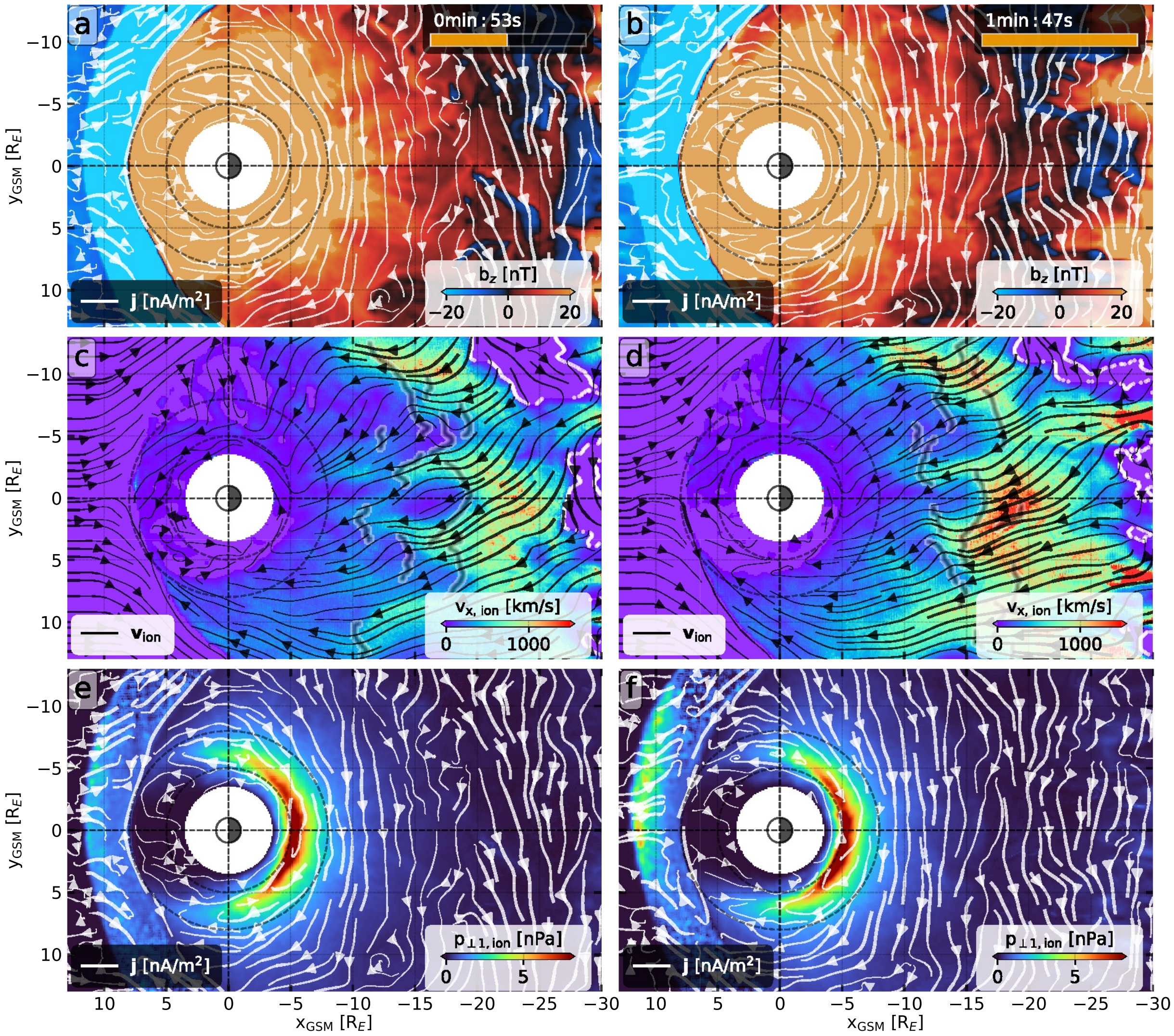

Figure 3. The top panels show a near-equatorial ($z_{GSM} = -0.05R_E$) cut of the B_z-component of the magnetic field (color coded) and the current density streamlines at 53 s (left) and 1 m 47 s. The middle panels show the ion flows in the x-direction and the flow streamlines (black on white). The lower panels contain a perpendicular component of the ion thermal pressure color coded and current density streamlines. The thickness of the current streamlines and flow streamlines gives an indication of their magnitude. The thick black lines in the middle panels show regions of dipolarization, and the white dots show flow reversals in v_x.

the reconnection regions are about 800 km/s. Earthward of the reconnection regions four relatively narrow regions of flow extend earthward. These correspond to BBFs. Two of the BBFs go toward the inner magnetosphere while the other two move toward the flanks of the magnetosphere. In Figure 3 at 1 m 47 s (middle, right), the ion flow velocity a couple of R_E earthward from the reconnection region has increased greatly to over 1,500 km/s. Near Earth, the flow has decreased to $\sim$200 km/s as the magnetic field increases. Note, the flow does not reverse direction near the tailward boundary for all the reconnection events. This occurs when the region of active reconnection is very near (one or two R_E) the boundary. The black lines in the middle panels indicate regions of enhanced B_z ($\Delta B_z > 2$ nT). They show earthward propagating dipolarizations. That there are several in one snapshot indicates the dynamic nature of the reconnection.

In the top panel of Figure 4, we have plotted one component of the perpendicular thermal pressure in addition to the current density streamlines. The current density vectors reverse direction from clockwise to counterclockwise across the region of enhanced ion pressure. This can be seen clearly in the middle and bottom panels of Figure 4. Here the peak in the pressure corresponds to a reversal in the current density mostly in the y_{GSM} direction indicating the diamagnetic current.

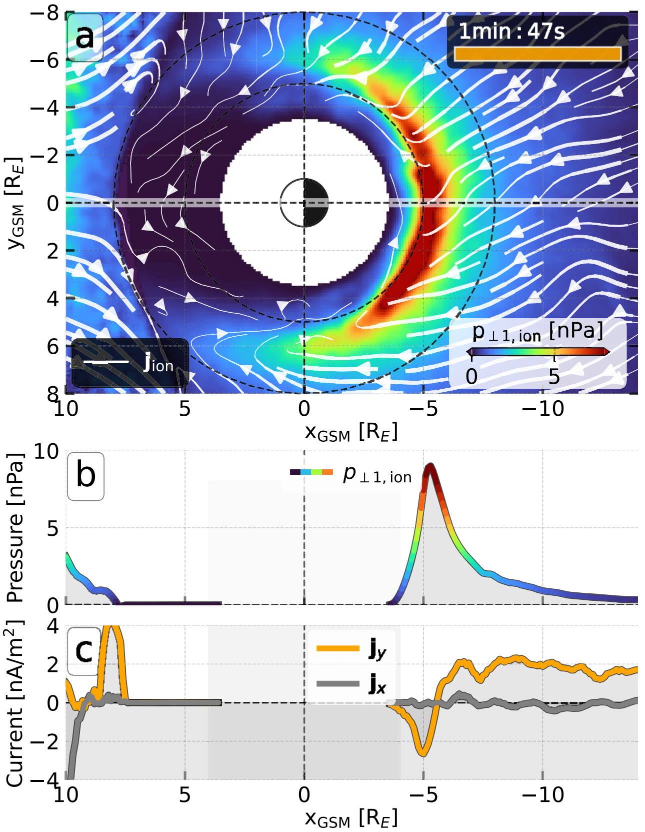

Figure 4. (top) One component of the perpendicular ion pressure color coded and current density streamlines near Earth at 1 m 47 s. The pressure along the noon-midnight line in the middle panel and j_x and j_y components of the current density are in the bottom panel. The thickness of the current streamlines gives an indication of their magnitude.

The top panels of Figure 5 give the $B_{y,\mathrm{GSM}}$ component of the magnetic field. In the region we have identified with reconnection, B_y is highly structured with areas of positive and negative B_y adjacent to each other. Similar structure occurs in $B_{x,\mathrm{GSM}}$ (not shown). Close examination of the currents in this region shows that this structure in B_y and B_x is associated with the locations of reconnection and by examining the parallel currents we find they delimit the reconnection regions. Although these two times are only 54 s apart, the pattern in B_y has changed indicating the variable nature of the PIC reconnection. Nearer to Earth in the region dominated by the dipole, $B_{y,\mathrm{GSM}}$ is negative at dawn and positive at dusk consistent with this plot being slightly below the equator.

The middle panels of Figure 5 give the electron velocities. At 53 s, the electron velocities away from the reconnection are much larger (>1500 km/s) than the ion velocities in the left middle panel of Figure 3. As noted above, by 1 m 47 s the ions have been greatly accelerated and earthward of $x_{\mathrm{GSM}} \sim -16R_{\mathrm{E}}$ the ions and electrons are moving at similar velocities. The flows in the reconnection region for both the electrons (Figure 5) and ions (Figure 3) are complex. El-Alaoui and Lapenta, et al. (2023), El-Alaoui and Walker, et al. (2023) argue that these flows are consistent with turbulence. However, when the flows narrow into the BBF-like structures at about $x_{\mathrm{GSM}} = -18R_{\mathrm{E}}$ both the electron and ion flows become more laminar. They are larger in the BBF than in the surrounding region.

The bottom panels of Figures 5 and 6 show the electron thermal pressure. The electron pressure is enhanced in the inner magnetosphere much as it was for the ions and similarly the largest pressures are found just tailward of the diamagnetic current. The electron pressures are smaller than the ion pressures (the electron peak pressure is half the ion pressure) but are not insignificant. The largest electron pressure is found from just before midnight to dawn, while the ion pressure is skewed toward dusk. This is consistent with the particles being heated during their drift motion.

We have separated the current densities in Figures 3–6 into the contributions from electrons and ions. The ion and electron velocities in Figures 3 and 5 are earthward but turn toward dusk and dawn respectively in the near-Earth region. The top panels of Figure 7 contain the resulting electron (left) and ion (right) current densities and current density streamlines. Combining them results in the current density plotted in the bottom panel. It also shows the ratio of electron to ion current densities.

Over most of the magnetosphere the electrons carry most of the current, however there are some places where the ions are important. In the tail the primary reconnection is carried by the electrons. Later we will show that in areas associated with secondary reconnection ion currents are significant (blue areas). Closer to Earth ions are important current carriers on the dusk side of the inner magnetosphere and in the diamagnetic current region.

The energy flux, **Q**, is given by

$$\mathbf{Q}_s(x,t) = \mathbf{q}_s + \overleftrightarrow{\mathbf{P}} \cdot \mathbf{u}_s + \mathbf{u}_s E_{\mathrm{th},s} + \mathbf{u}_s \rho_s \mathbf{u}_s^2/2 \tag{1}$$

where $\mathbf{q}_s$ is the heat flux, $\overleftrightarrow{\mathbf{P}}$ is the pressure tensor, $\mathbf{u}_s$ is velocity, $E_{\mathrm{th},s}$ is the thermal energy, and ρ_s is the mass density for a species s. The total ion energy flux is plotted in Figure 8. The top panels give the total energy flux, while the middle panels give the kinetic energy fluxes and the bottom panels the combined heat and enthalpy fluxes. Again, the color coding shows the magnitude and the arrows the direction. The energy fluxes in Figures 8 and 9 have been smoothed by using the same Gaussian smoothing as the current density. The enhanced energy flux from reconnection at both times moves earthward from the reconnection region along the BBF-like structures. As the reconnection continues, the earthward energy flux in the tail grows with the largest energy flux in the

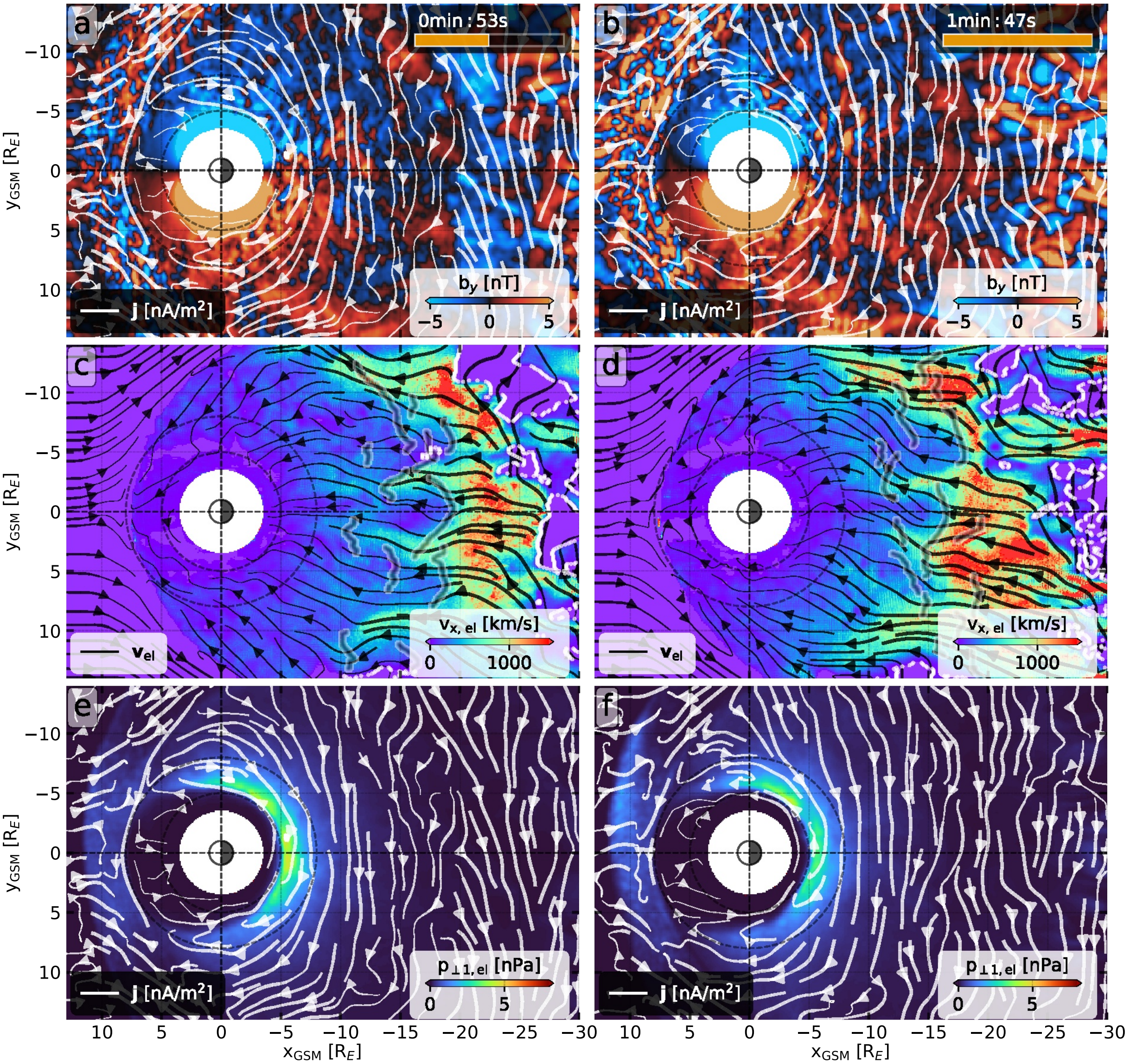

Figure 5. (top) $B_{y,\mathrm{GSM}}$ component of the magnetic field and current density streamlines near the equatorial plane at 53 s (left) and 1 m 47 s (right). The middle panel contains the x-component of the electron velocity and velocity streamlines while the bottom panel contains one component of the perpendicular pressure (color coded) and the current density streamlines. The thick black lines in the middle panels show the main regions of dipolarization, and the white dots show flow reversals in v_x.

BBF on the dusk side. Notice that the dusk-side energy flux is diverted toward dusk at about $x_{\mathrm{GSM}} = -20R_{\mathrm{E}}$. Similar behavior can be seen in the flows in Figure 3. The largest energy flux is in the region of the ring current and is directed clockwise. It is larger pre-midnight than post-midnight. It can be seen in Figure 8 (right) that the plasma from the tail reconnection contributes to the energy flux in the partial ring current at $x_{\mathrm{GSM}} \approx -10R_{\mathrm{E}}$ and $y_{\mathrm{GSM}} \approx \pm 2R_{\mathrm{E}}$ where the energy flux in the two BBFs turns duskward and joins with the rest of the partial ring current. While the ion energy flux is directed from dawn to dusk in most of the inner magnetosphere, it reverses in the diamagnetic region.

The kinetic energy flux is largest in the earthward flows from the reconnection region. It increases in regions of greater ion velocity. The combined heat flux and enthalpy flux (the first three terms in Equation 1) for the two times are on the bottom. Generally, the enthalpy flux (the second and third terms) is much larger than the heat flux (see Lapenta et al., 2020). As time increases, the energy flux in the tail grows. The growth between 53 s and 1 m 47 s results from the increase in ion velocity noted in Figure 3. The kinetic energy flux is largest in the tail, but the

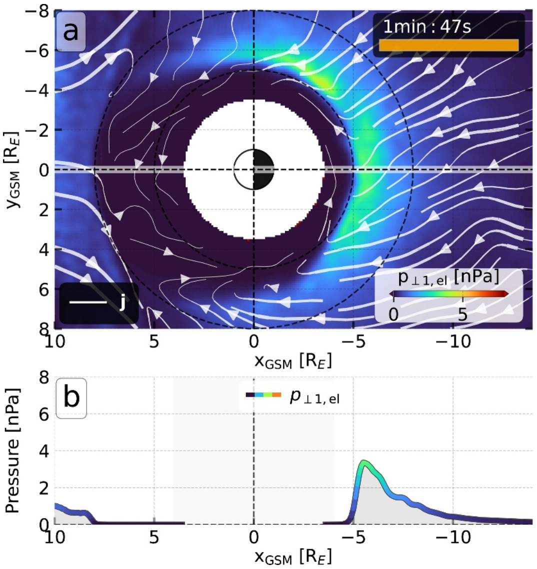

Figure 6. (top) One component of the perpendicular electron pressure color coded and current streamlines near Earth. The pressure (nPa) along the noon-midnight line is in the bottom panel. The thickness of the current density streamlines gives a measure of the magnitude of the current density.

enthalpy flux is also significant. However, at both times, closer to Earth, the combined heat flux and enthalpy flux dominate. As the BBFs propagate earthward, the heat flux and enthalpy flux grow and are much larger than the kinetic energy flux.

Figure 9 shows the energy flux for electrons. Like the ions, the electron energy flux is the largest in the inner magnetosphere but in the dawn quadrant. However, electron energy fluxes are smaller than the ion energy fluxes (note the scale has been reduced from that in Figure 8). In the reconnection region $(x_{\mathrm{GSM}} < -15R_{\mathrm{E}})$, kinetic energy flux is earthward and toward dawn $(y_{\mathrm{GSM}} < 0)$. The electron enthalpy flux and heat flux are tailward and toward dusk. As was the case for the ions, near Earth the enthalpy flux and heat flux are larger than the kinetic energy flux for the electrons.

3.2. Analysis of Ion Trajectories

In Figure 10, we plot the trajectories of 10,000 randomly selected ions from the PIC simulation starting in the region where the reconnection occurs $(x_{\mathrm{GSM}} < -15R_{\mathrm{E}})$. The selection was limited to $-10R_{\mathrm{E}} < y_{\mathrm{GSM}} < 10R_{\mathrm{E}}$ and $-1R_{\mathrm{E}} < z_{\mathrm{GSM}} < 1R_{\mathrm{E}}$ to include the source of the BBF closest to midnight and to initial energies of less than 20 keV. Figure 10 shows the particle trajectories at four times from near the beginning of the simulation cycle 2,000 (1 s) to cycle 202,500 (1 m 47 s), which was the end of the simulation. It should be noted these are the trajectories of actual ions from the simulation and not test particles. The panel on the left is a 3D view of the trajectories and on the right is the view projected onto the equatorial plane. As the calculation proceeds, the individual particle traces are shown in black, saturating in regions where there are many overlapping particles. Ions moving along field lines and mirroring are evident in the time series especially between 53 and 82 s. The trajectory plots show that the ions reach the inner magnetosphere and that they sort themselves into the two clear BBFs. The ions initially have a mean energy of about 10 keV and end up with ~20 keV, but there is a wide range with 90% of the ions between 5 and 42 keV. Two movies showing the time series of the ions moving toward Earth have been included in the supplementary material.

Reconnection in the MHD simulation occurs along a neutral line extending across the tail (as illustrated in Figure 1). As time progresses, the reconnection develops a much more complex pattern in the PIC simulation. Examination of $B_{z,\mathrm{GSM}}$ and $B_{y,\mathrm{GSM}}$ in Figures 3 and 5 suggests a pattern such that the plasma from the reconnection in the more distant tail is subject to further reconnection as it moves earthward. In Figure 11, we show field lines calculated in the region of reconnection near $y_{\mathrm{GSM}} = 3R_{\mathrm{E}}$. The field lines show three or four regions of reconnection. One is located near the tailward boundary and possibly another just earthward of that at about $x_{\mathrm{GSM}} = -29R_{\mathrm{E}}$, one at about $x_{\mathrm{GSM}} = -25R_{\mathrm{E}}$ and one at about $x_{\mathrm{GSM}} = -19R_{\mathrm{E}}$. The BBF on the dusk side originates near the two more earthward reconnection sites. They are secondary reconnection sites on closed field lines.

In the next three figures, we examine the acceleration of the ions as they move earthward. We selected 30 particles from Figure 10 to examine in greater detail. In Figure 12, we follow the trajectory of an ion that starts at about $x_{\mathrm{GSM}} = -25R_{\mathrm{E}}$ and $y_{\mathrm{GSM}} = -7R_{\mathrm{E}}$ with an energy of a few keV. This is located just earthward of a region of reconnection in Figure 3. The ion gains energy there and then meanders across the tail (starting at 20 s) slowly gaining energy. The rate of energization increases when the particle encounters reconnection at about $x_{\mathrm{GSM}} = -20R_{\mathrm{E}}$ and $y_{\mathrm{GSM}} = 3R_{\mathrm{E}}$. This is the earthward-most reconnection site in Figure 11. The radius of curvature of the field line becomes small just earthward of this reconnection site (Figure 11) and the ion is scattered along the magnetic field (Ashour-Abdalla et al., 2005). It mirrors at about $x_{\mathrm{GSM}} = -8R_{\mathrm{E}}$. Overall this ion gains about 30 keV, most of it in the near-Earth region of reconnection as seen in Figures 3 and 11. The energization is not uniform. Panel (d) shows that during the interval when the ion meanders across the tail, it alternatively gains and loses energy with an overall net gain. While most of the energization is perpendicular to the magnetic field, there are brief intervals when the particle is accelerated and decelerated by parallel electric fields. This is an example of a particle that gains most of its energy in the reconnection region at the start of the dusk side BBF.

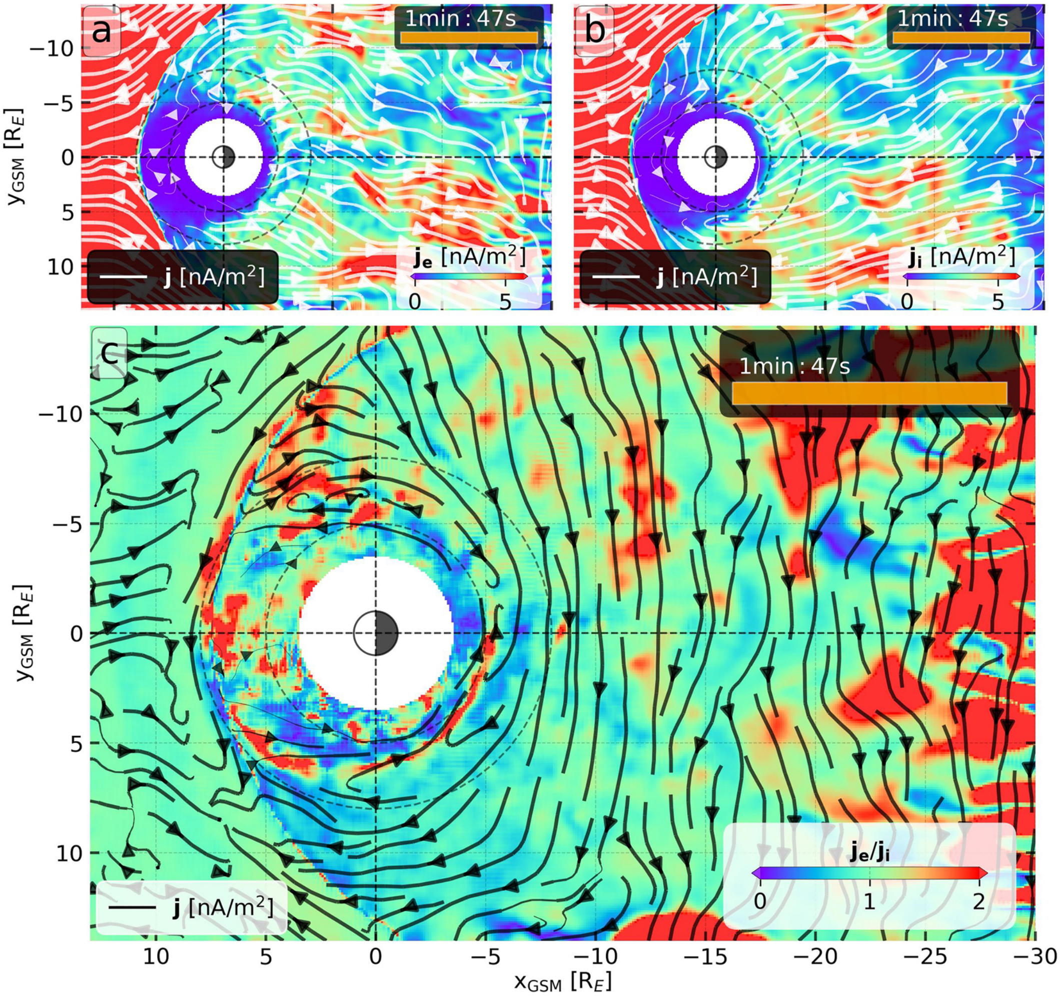

Figure 7. The electron current (a) and the ion current (c) at 1 m 47 s. Panel (c) shows the ratio of electron to ion current, $\mathbf{j_e}/\mathbf{j_i}$. The black streamlines show the direction of the net current.

Figure 13 shows an ion that, like the one in Figure 12, started in the dawn side reconnection region. It too follows a non-adiabatic trajectory across the tail to the dusk side where it is energized by reconnection in the region nearer the tailward edge of the simulation. At 40 s, the ion encounters strong parallel electric fields (panel d) near the tail most reconnection site and gains several keV. It encounters several intervals with parallel electric fields between 40 s and ∼75 s before it interacts with the series of reconnection sites near $y_{\mathrm{GSM}} = 3R_{\mathrm{E}}$. Note that as it passes through the reconnection region it is alternately accelerated and decelerated (panel d). It emerges with about 90 keV. It too is scattered along the field in the region with a small radius of curvature (panel c).

Many of the ions in Figure 10 start out with large pitch angles. The ion in Figure 14 starts at $x_{\mathrm{GSM}} \sim -20R_{\mathrm{E}}$, $y_{\mathrm{GSM}} \sim 2R_{\mathrm{E}}$ with a small pitch angle. It mirrors and returns to the equator at about $x_{\mathrm{GSM}} = -12R_{\mathrm{E}}$. Note that once it returns to the equator it has a large pitch angle and encounters a dipolarization front shown in red. It then drifts across the tail toward dusk and gains energy. This particle also has non-adiabatic motion across the tail.

These three ions are typical of the 30 we examined in detail and are consistent with the ions in the sample of 10,000 (This is especially evident in the movies in the supplementary material.) The major acceleration occurs when the ion is in the regions of reconnection in Figure 3. Between the reconnection regions they move on non-adiabatic orbits. They can gain energy at the dipolarization fronts. Earthward of about $x_{\mathrm{GSM}} = -12R_{\mathrm{E}}$ ions drift across the electric field and gain energy adiabatically.

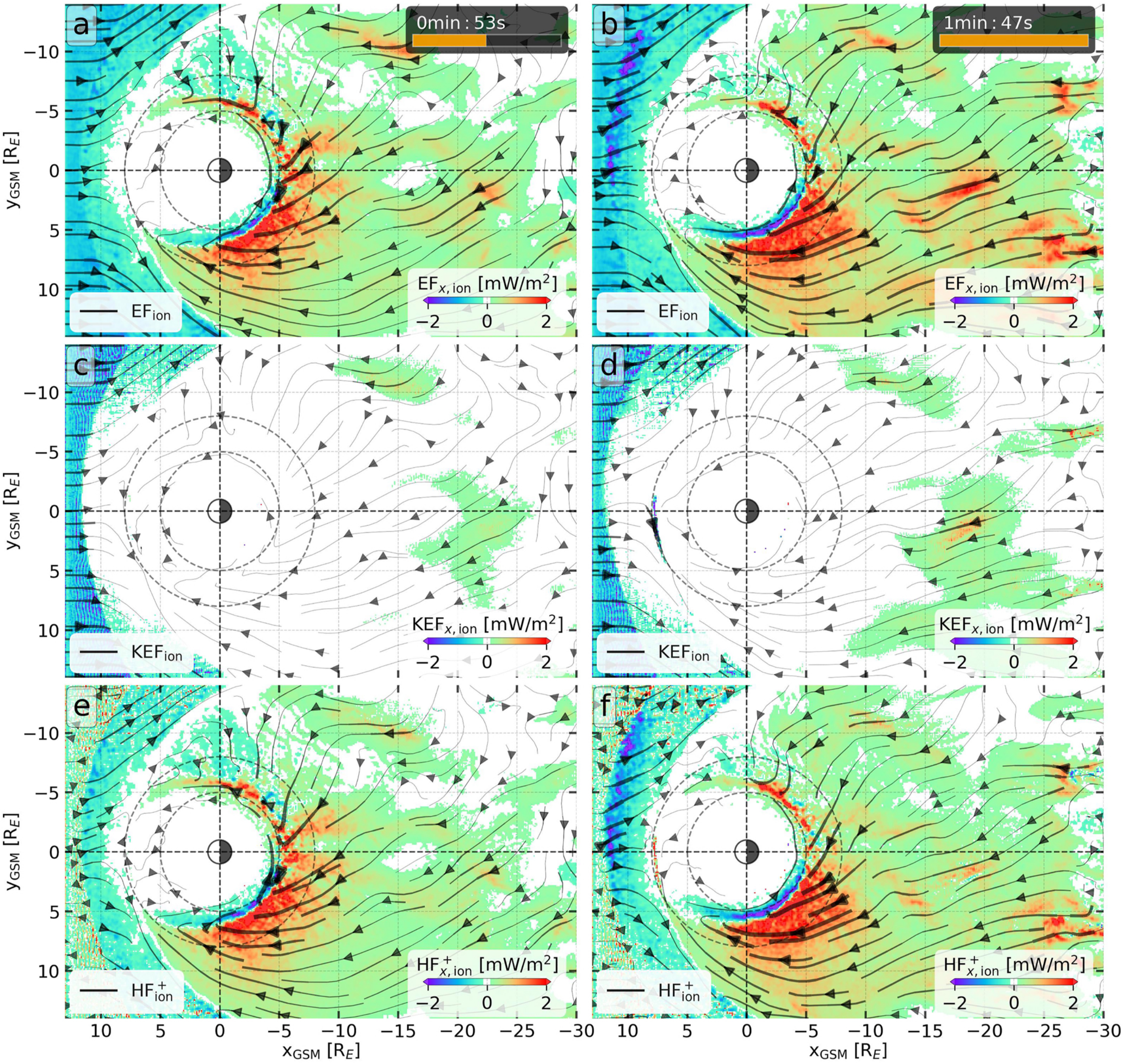

Figure 8. (top) The x-component of the total ion energy flux at 53 s (left) and 1 m 47 s (right). The middle panels contain the x-component of the kinetic energy flux and the bottom panels contain the x-component heat flux and enthalpy flux together. The thickness of the energy flux streamlines gives an indication of their magnitude.

4. Discussion

We have used a combination of a global MHD simulation and a particle-in-cell (PIC) simulation to model the flow of energy and plasma from magnetotail reconnection regions into the inner magnetosphere and the formation of a partial ring current. The first question we needed to address in this study is can we use the PIC and MHD simulation to model plasma from the magnetotail reconnection to the inner magnetosphere. The 10,000 ions in Figure 10 show that ions which experienced reconnection tailward of $x_{\mathrm{GSM}} = -15R_{\mathrm{E}}$ reach the inner magnetosphere. At the end of simulation, particles which encountered reconnection had equatorial crossing distances $x_{\mathrm{GSM}} < -8R_{\mathrm{E}}$. The simulation contains many expected properties of the region between the region of tail reconnection for $x_{\mathrm{GSM}} < -18R_{\mathrm{E}}$ and the inner magnetosphere including the ring current and diamagnetic current. This enables us to study the acceleration of particles enroute to the inner magnetosphere.

The use of the PIC simulation allows the inclusion of physical processes not found in other approaches. Even though the electron inertial length is not fully resolved (Figure 2), the PIC code still includes physics not contained in hybrid models since the electrons (as well as the ions) can gradient and curvature drift in the magnetic field, and

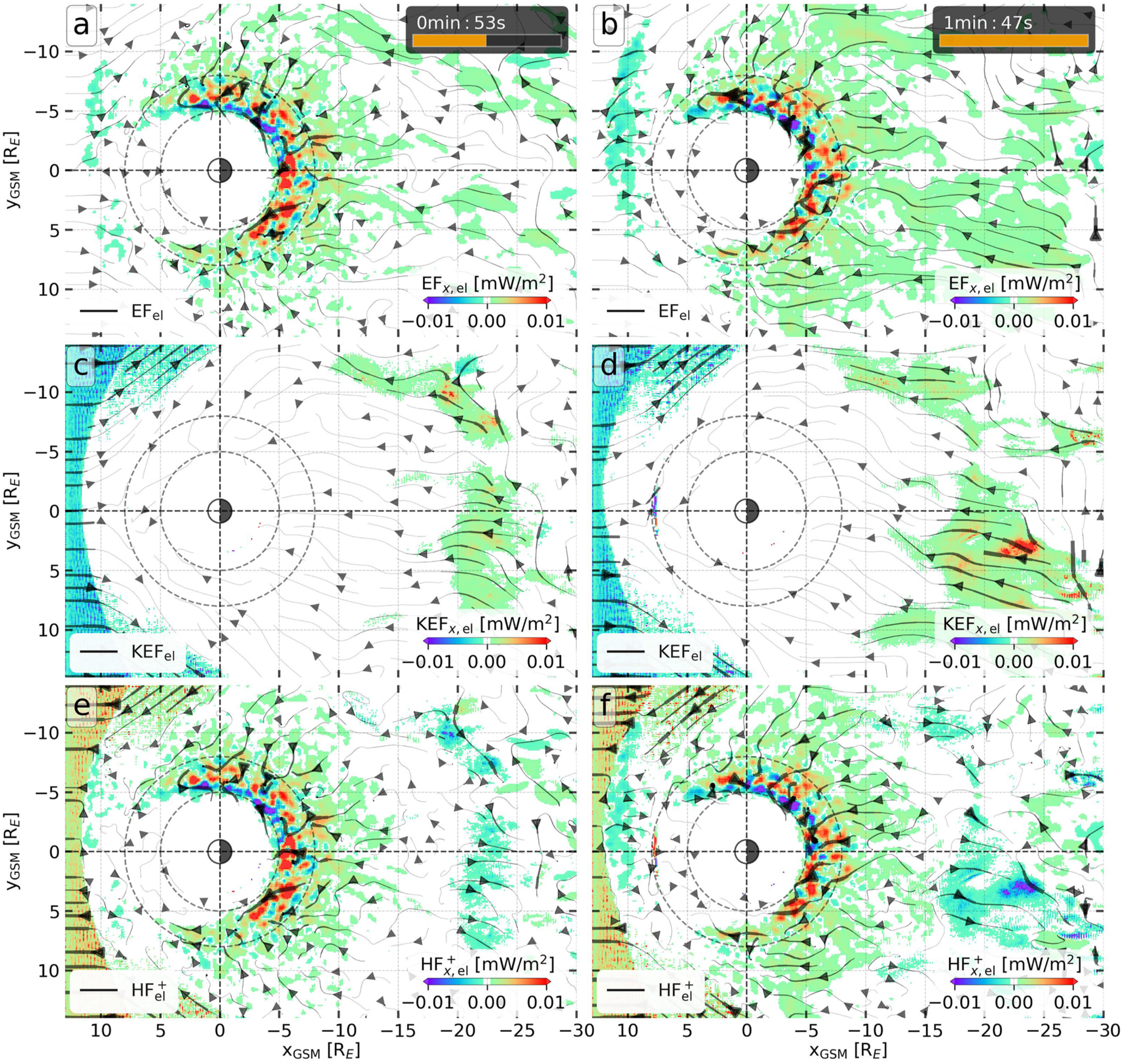

Figure 9. (top) The x-component of the electron energy flux color coded and streamlines showing the x- and y- components of the energy flux at 53 s (top, left) and 1 m 47 s (top, right). The middle panels show the kinetic energy fluxes, and the bottom panels show the combined enthalpy flux and heat fluxes. Note the scale for the energy flux is smaller than that in Figure 8 The thickness of the energy flux streamlines gives an indication of their magnitude.

the electron gyration is resolved in most regions of the simulation. In Figure 9, we found that the electron energy flux distribution is skewed toward dawn while in Figure 8 the ion energy flux is largest toward dusk, indicative of adiabatic acceleration in the near-Earth region.

The electrons stream away from the reconnection site much faster than the ions (Figures 3 and 5). However, when the particles are a few R_E from the reconnection site, both electrons and ions are moving at approximately the same velocity $(\mathbf{E} \times \mathbf{B}/B^2)$ until they get closer to Earth where drift effects become important. The initial difference in the flow away from the reconnection region creates an ambipolar electric field that decelerates the electrons and accelerates the ions (Aunai et al., 2011; Lapenta et al., 2016). The jetting of plasma from the reconnection regions is primarily in the x_{GSM} direction. We have examined the differences between the ion and electron flows away from the reconnection in detail to determine the distance over which this occurs. The ions' x-component of velocity approximately matches that of the electrons over distances of $\sim 10 d_i$ earthward of the reconnection site. This is the scale size of the ion diffusion region (e.g., Yamada et al., 2010).

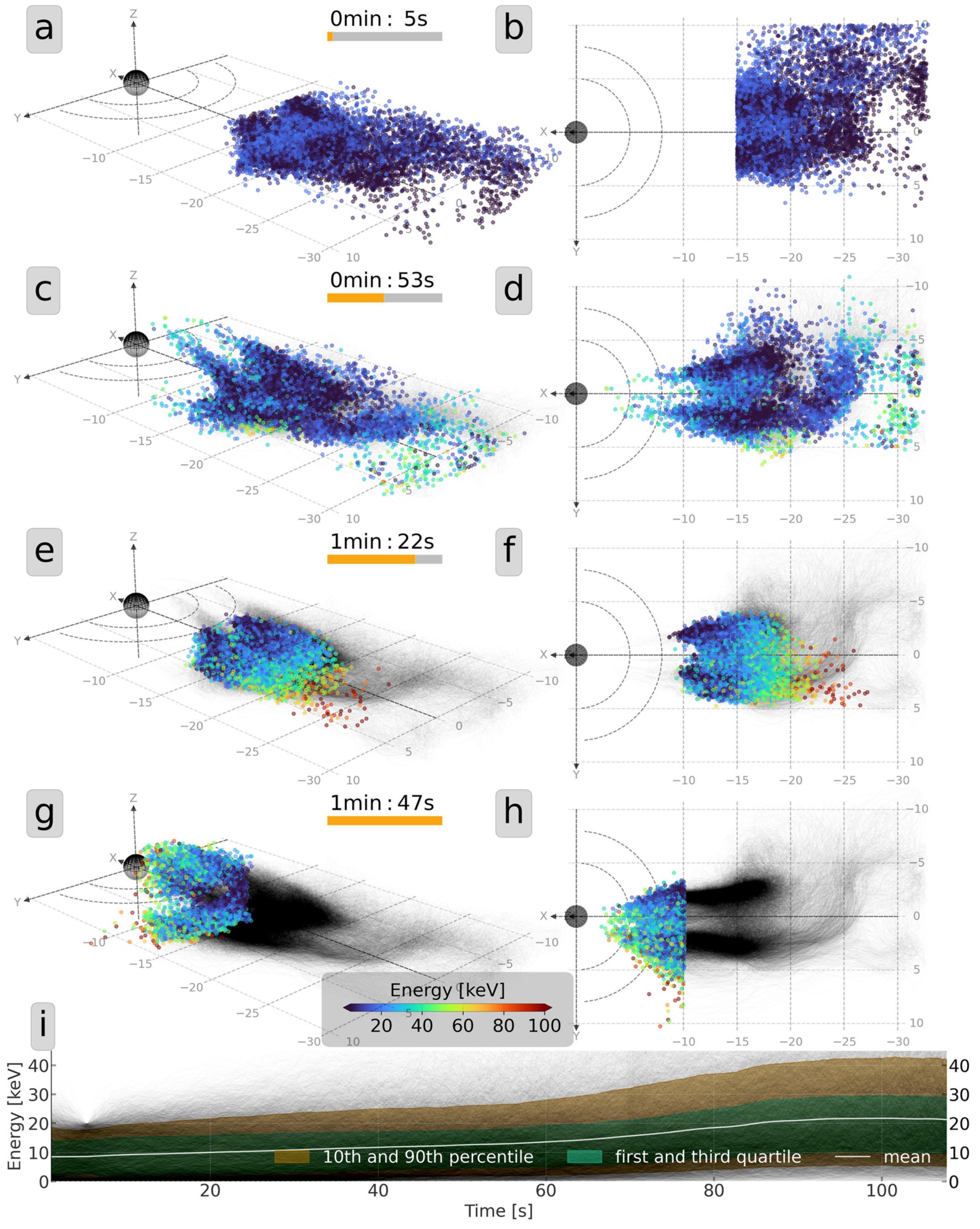

Figure 10. The trajectories of 10,000 randomly selected ions from the simulation (color coded by energy) starting 1 s into the simulation and ending at the end of the simulation (1 m 47 s). The particles were selected from a region $x_{\mathrm{GSM}} < -15R_{\mathrm{E}}$, $-10R_{\mathrm{E}} < y_{\mathrm{GSM}} < 10R_{\mathrm{E}}$, $-1R_{\mathrm{E}} < z_{\mathrm{GSM}} < 1R_{\mathrm{E}}$ and with initial energies of less than 20 keV. The left panels show a 3D projection of the trajectories while the right panels give an equatorial view, with particle traces shown in black. The individual particles have been color coded with energy. The dashed semicircles are at $R = 8R_{\mathrm{E}}$ and $5R_{\mathrm{E}}$. The panel on the bottom gives the mean energy of the ions (white curve), 10th and 90th percentiles (brown) and the lower and upper quartiles (green).

As the plasma moves from the reconnection region, the flows narrow into BBF-like structures. The energy flux from reconnection initially is mostly in the form of kinetic energy flux. The results from the simulation are consistent with observations. Cao et al. (2013) presented Cluster observations of the ion kinetic energy flux associated with BBFs. They found between 1 and 4 mW/m^2 while we found about 1–2 mW/m^2 as shown in Figure 8. As the BBFs move toward the inner magnetosphere, the ion energy flux changes to primarily internal

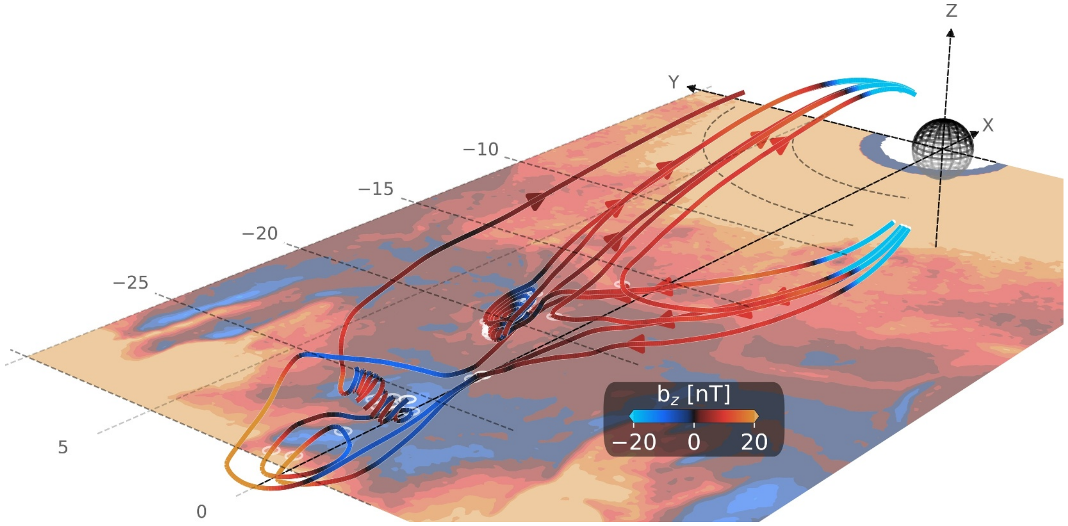

Figure 11. Field lines calculated at time at 1 m 47 s in the dusk region near $y_{\mathrm{GSM}} = 3R_{\mathrm{E}}$. A plot of $B_{z,\mathrm{GSM}}$ in the equatorial plane shows the relationship of these field lines to the overall pattern of reconnection. The color coding gives the value for $B_{z,\mathrm{GSM}}$.

energy flux in the form of enthalpy flux (Figure 8). We have integrated the energy flux in the BBF near Earth to calculate the power delivered to the inner magnetosphere from the ions. The integration was carried out for a BBF crossing the plane at $x_{\mathrm{GSM}} = -12R_{\mathrm{E}}$. This is near their closest approach to Earth before there is appreciable drift duskward. At 1 m 47 s, the region near midnight where two of the BBF are found delivers 2×10^{11} W. Angelopoulos et al. (1994) estimated that the power to the ring current region is 3×10^{11} W with $\sim 2.7 \times 10^{10}$ W in a BBF. We included only the region closest to midnight since this is the region where particles from the tail reach the inner magnetosphere in Figure 3.

We also examined the electron energy flux. Like the ions, the energy flux in the electrons is mostly kinetic energy flux in the reconnection region. However, in places the enthalpy and heat fluxes are tailward even when the kinetic energy flux is positive (Figure 9). In an earlier study, we found that with a single reconnection site in the tail both the kinetic energy flux and the enthalpy flux were tailward (Lapenta et al., 2020). The largest tailward enthalpy flux in Figure 9 is earthward of $x_{\mathrm{GSM}} = -24R_{\mathrm{E}}$ and at $y_{\mathrm{GSM}} = 3R_{\mathrm{E}}$. This is the region of secondary reconnection in Figure 11. A plausible explanation is that the secondary reconnection does not greatly alter the earthward flow (Figure 5) but is sufficient to reverse the enthalpy and heat fluxes.

We initially assumed an ion to electron temperature ratio of 5. As the simulation evolved it changed. We have examined the ratio of ion to electron temperatures in snapshots at various times during the simulation. We calculated the temperatures from the diagonal element of the pressure tensor and examined temperatures based on the individual elements and the trace (see Lapenta et al., 2016). For instance, at 1 m 47 s the temperature ratio in the reconnection region varies from 2 to 15. The largest temperature ratio occurred in an area of reconnection, duskward of midnight where we find the largest earthward ion energy flux in Figure 8. Wang et al. (2012) report ratios between 5 and 10 based on a statistical study. Closer to Earth, within $7R_{\mathrm{E}}$ or $8R_{\mathrm{E}}$, the ions reach 50 keV in the simulation. The largest ion temperature is found in the pre-midnight region. Electron temperatures reaching 15 keV are found primarily post-midnight. Close to Earth and on the dusk side the ion to electron temperature ratio is 4–15, while on the dawn side it is 2–4.

The region in the tail with multiple sites of reconnection is characterized by flow vorticity suggestive of turbulence. In MHD simulations, plasma in a BBF flows earthward in a region with heightened vorticity (Figure 1) (see El-Alaoui et al., 2021, for a review of vorticity and turbulence in global MHD simulations of the magnetosphere). However, in the PIC simulation the vorticity decreases, and the flow streamlines in Figures 3 and 5 appear more laminar. If turbulent acceleration is important, the simulation results indicate that it is occurring in the region with multiple reconnection sites tailward of $x_{\mathrm{GSM}} \sim -16$ to $-18R_{\mathrm{E}}$. The possibility of turbulent acceleration was suggested by Ergun et al. (2022) based on observations and Lapenta et al. (2020) based on a

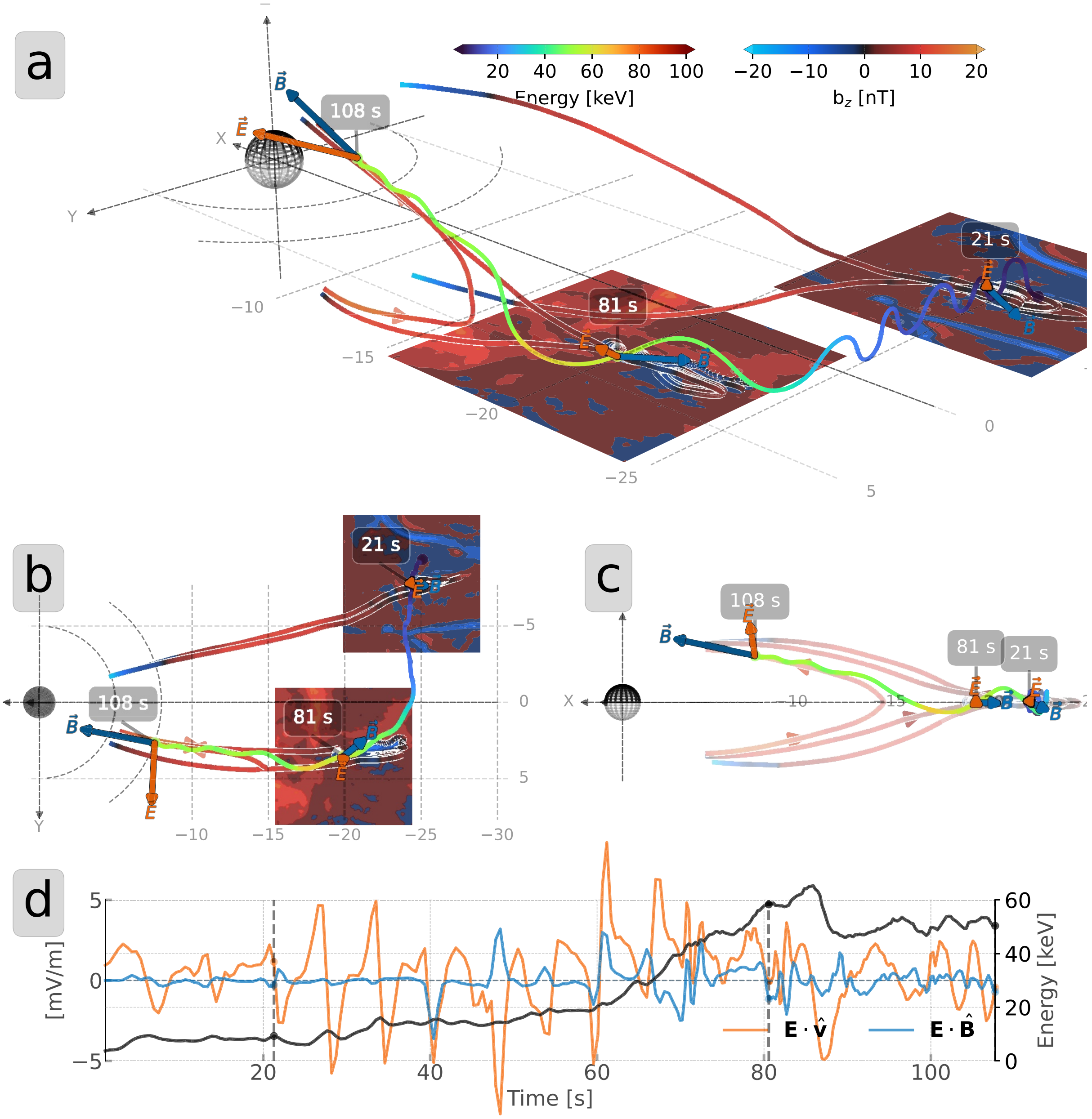

Figure 12. The trajectory of an ion that gains most of its energy by interaction with secondary reconnection where the dusk-side BBF starts. Panel (a) gives a 3D rendering of the trajectory. The particle is color coded with particle energy. Sections of the trajectory have a region just below the equatorial plane color coded with the $b_{z,\mathrm{GSM}}$ component of the magnetic field. At selected times, the instantaneous magnetic field vector is given by a blue arrow and the electric field is given by an orange arrow. The time in seconds is in white. Magnetic field lines at selected locations are in the color of $b_{z,\mathrm{GSM}}$ and are outlined in white. Panel (b) is an equatorial view of the ion. Panel (c) is a $x_{\mathrm{GSM}}/z_{\mathrm{GSM}}$ projection of the ion trajectory. Panel (d) gives the energy of the ion as a function of time (black). The same panel shows $\mathbf{E}\cdot\hat{\mathbf{v}}$ in orange where $\mathbf{E}$ is the electric field and $\hat{\mathbf{v}}$ is a velocity unit vector and $\mathbf{E}\cdot\hat{\mathbf{B}}$ in blue where $\hat{\mathbf{B}}$ is a magnetic field unit vector.

magnetotail simulation using the iPic3D code; it should be noted that the magnetotail PIC simulation in Lapenta et al. (2020) like this one does not have sufficient resolution to fully resolve turbulent heating, especially for the electrons. This will require a higher resolution calculation that is beyond the scope of this paper. A recent paper by Richard et al. (2023) investigated ion dynamics in plasma jetting away from the reconnection. The authors argue that the ion distributions are isotropized by non-adiabatic motion of the untrapped particles like that seen in Figures 12–14.

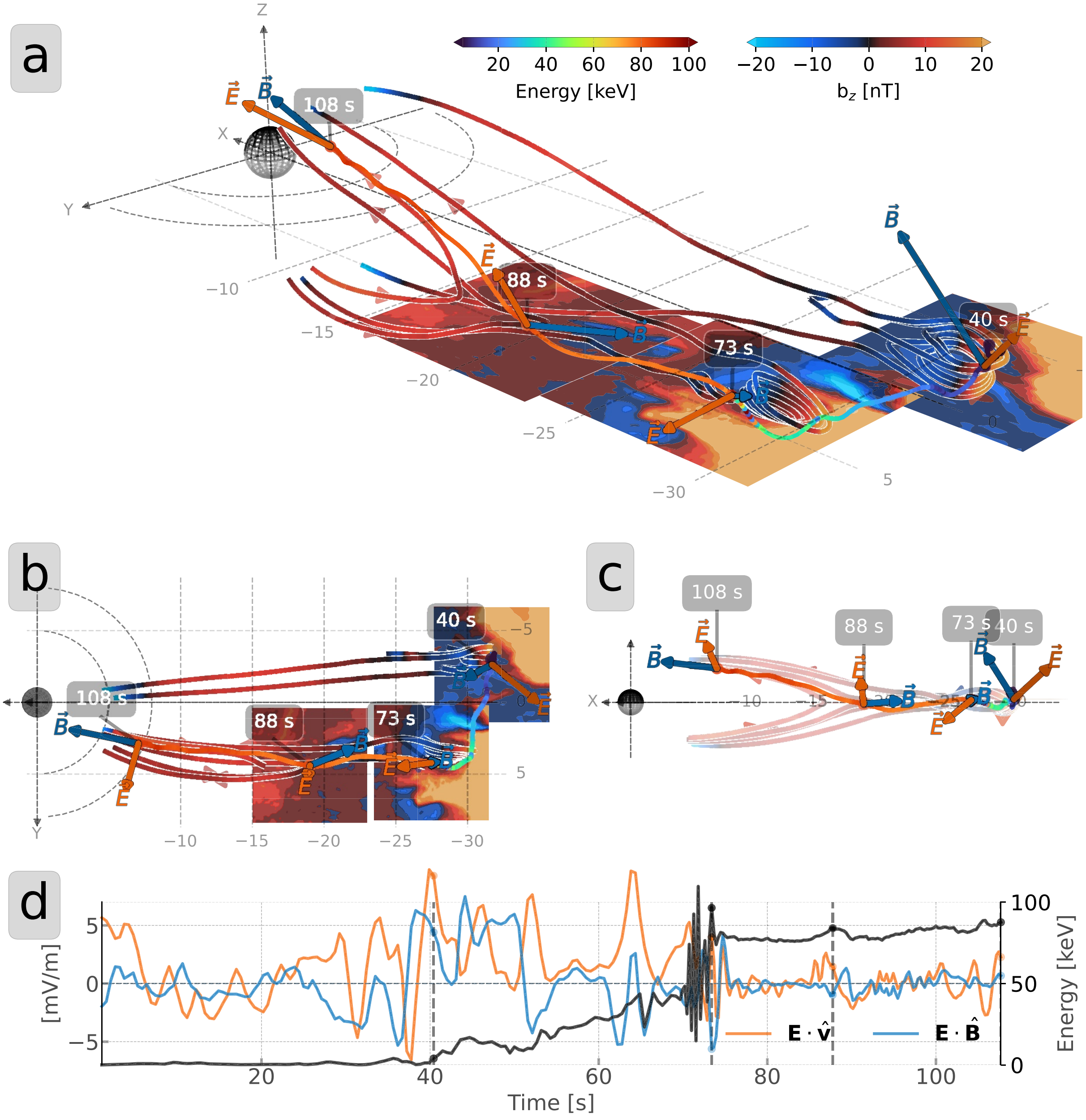

Figure 13. The trajectory of an ion which is accelerated when it passes through the flux rope near the more distant reconnection site. The format is the same as in Figure 12.

As the simulation proceeds, a partial ring current and diamagnetic current form for $x_{GSM} < -10R_E$. Initially, this results from gradient and curvature drift of the particles loaded into the simulation. However, at later times in the simulation, particles from magnetotail reconnection contribute to the energy flux near Earth (see Figure 8). The thermal pressure in the ring current region is enhanced. By the end of the simulation, the average energy of the ions for $x_{GSM} > -10R_E$ was about 20 keV, but they ranged between 5 and 42 keV (Figure 10).

The plasma from reconnection in the magnetotail can be accelerated in several ways en route to the inner magnetosphere. There can be additional reconnection sites and plasma acceleration at the dipolarization fronts. The ions in Figures 12–14 are representative of some of the forms of acceleration. We found that the ions gained most of their energy when they interacted directly with reconnection. Both the primary reconnection and secondary reconnections (Figure 11) are involved in the energization. When the ions were near Earth and drift effects

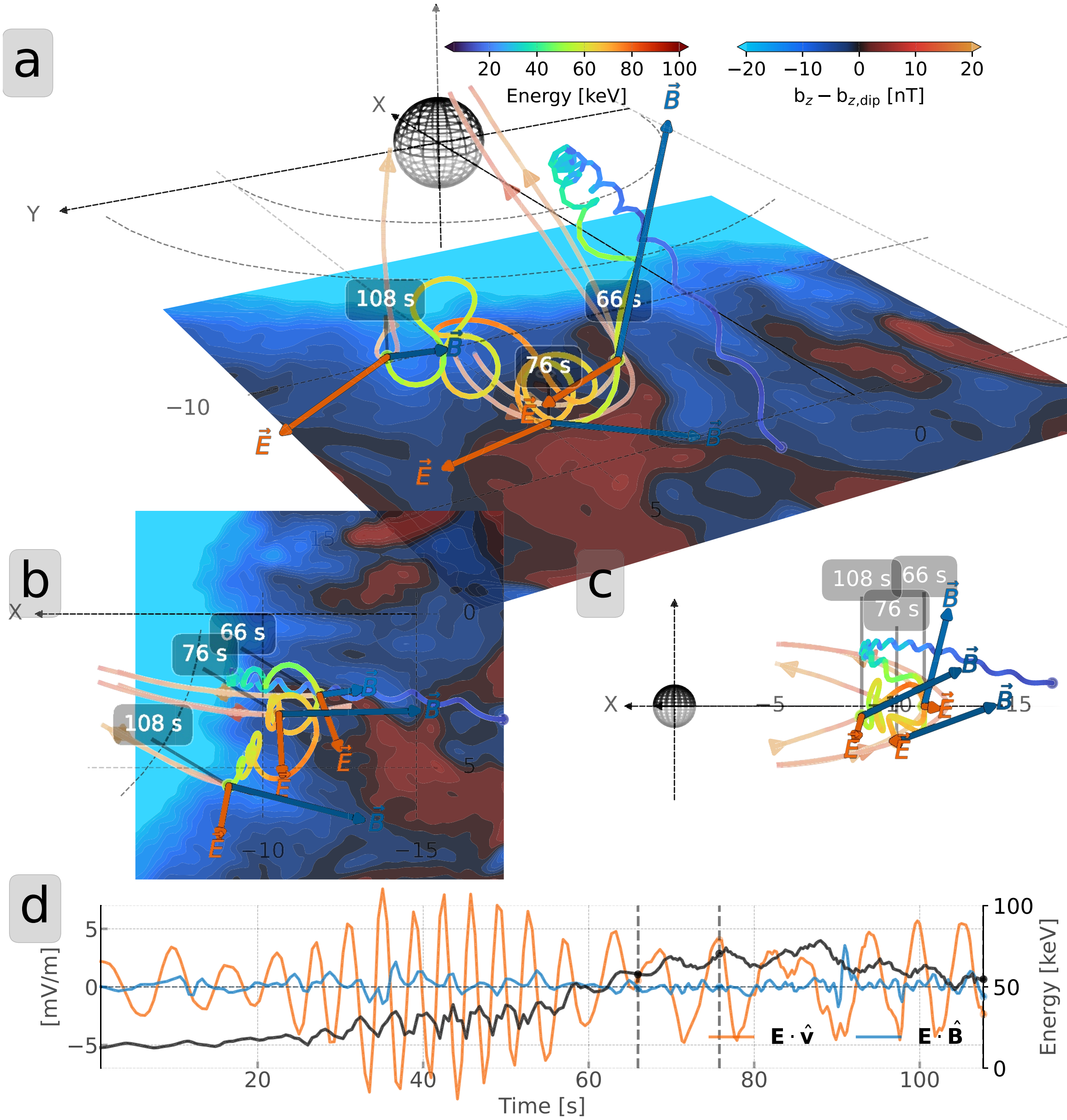

Figure 14. An ion that starts just duskward of midnight with a small pitch angle. The background shows $B_{z,\text{GSM}} - B_{z,\text{dip}}$. Otherwise, the format is the same as in Figure 12.

became more important, they gained further energy. As the ions moved between the reconnection sites they were untrapped and moved on non-adiabatic meandering orbits.

5. Conclusions

The feasibility of combining a PIC simulation with a global MHD simulation that includes the magnetotail and inner-Earth region has been demonstrated in the global model described in this paper. We show the formation of a partial ring current and diamagnetic current. By the end of the calculation, particles from the magnetotail reconnection region reach the inner magnetosphere where they can contribute to the partial ring current. The largest sources of the particles to the inner magnetosphere relate to BBFs that originate from a complex pattern of reconnection in the near-Earth magnetotail. The ions in the simulation gain most of their energy in this complex reconnection region. They gain additional energy close to Earth where they can drift across the electric field. The initial energy flux in the BBFs is mainly in the form of kinetic energy flux from the jetting particles, but as they move closer to the ring current the energy flux changes to enthalpy flux. The energy flux from the simulation is consistent with observations in the inner magnetosphere.

Data Availability Statement

The Python model analysis software and scripts to generate the figures are provided in Rusaitis (2024b) and are hosted on GitHub at https://github.com/rusaitis/2024-Ring-Current-Paper under the Massachusetts Institute of Technology (MIT) license. The necessary simulation data to reproduce the results in the paper are hosted on Zenodo (Rusaitis, 2024a). The iPic3D particle-in-cell code is available on GitHub at https://github.com/CmPA/iPic3D. Figures were made with Matplotlib version 3.8.4 (Team, 2024), available under the Matplotlib license at https://matplotlib.org.

Acknowledgments

LR, ME, and RJW received funding from the NSF award NSF2040319. GL received funding from the ERC Advanced Grant TerraVirtuale (grant agreement No. 1101095310). Views and opinions expressed are however those of the authors only and do not necessarily reflect those of the European Union or the European Commission. Neither the European Union nor the European Commission can be held responsible for them. The MHD and PIC computations were performed by GL, ME, and LR using the Pleiades supercomputer housed at the NASA Advanced Supercomputing (NAS) facility at NASA's Ames Research Center.

References

Angelopoulos, V., Baumjohann, W., Kennel, C. F., Coroniti, F. V., Kivelson, M. G., Pellat, R., et al. (1992). Bursty bulk flows in the inner central plasma sheet. *Journal of Geophysical Research*, *97*(A4), 4027–4039. https://doi.org/10.1029/91JA02701

Angelopoulos, V., Kennel, C. F., Coroniti, F. V., Pellat, R., Kivelson, M. G., Walker, R. J., et al. (1994). Statistical characteristics of Bursty bulk flow events. *Journal of Geophysical Research*, *99*(A11), 21257–21280. https://doi.org/10.1029/94JA01263

Ashour-Abdalla, M., Bosqued, J. M., El-Alaoui, M., Peroomian, V., Zelenyi, L. M., Walker, R. J., et al. (2005). A stochastic sea: The source of plasma sheet boundary layer ion structures observed by Cluster. *Journal of Geophysical Research*, *110*(A12), A12221. https://doi.org/10.1029/2005JA011183

Aunai, N., Belmont, G., & Smets, R. (2011). Proton acceleration in antiparallel collisionless magnetic reconnection: Kinetic mechanisms behind the fluid dynamics: Proton dynamics in magnetic reconnection. *Journal of Geophysical Research*, *116*(A9), A09232. https://doi.org/10.1029/2011JA016688

Baumjohann, W., & Paschmann, G. (1989). Average plasma properties in the central plasma sheet. *Journal of Geophysical Research*, *94*(A6), 6597–6606. https://doi.org/10.1029/JA094iA06p06597

Cao, J., Ma, Y., Parks, G., Reme, H., Dandouras, I., & Zhang, T. (2013). Kinetic analysis of the energy transport of Bursty bulk flows in the plasma sheet. *Journal of Geophysical Research: Space Physics*, *118*(1), 313–320. https://doi.org/10.1029/2012JA018351

Chen, Y., & Tóth, G. (2019). Gauss's law satisfying energy-conserving semi-implicit particle-in-cell method. *Journal of Computational Physics*, *386*, 632–652. https://doi.org/10.1016/j.jcp.2019.02.032

Cramer, W. D., Raeder, J., Toffoletto, F. R., Gilson, M., & Hu, B. (2017). Plasma sheet injections into the inner magnetosphere: Two-way coupled OpenGGCM-RCM model results. *Journal of Geophysical Research: Space Physics*, *122*(5), 5077–5091. https://doi.org/10.1002/2017JA024104

De Zeeuw, D. L., Sazykin, S., Wolf, R. A., Gombosi, T. I., Ridley, A. J., & Tóth, G. (2004). Coupling of a global MHD code and an inner magnetospheric model: Initial results. *Journal of Geophysical Research*, *109*(A12), 2003JA010366. https://doi.org/10.1029/2003JA010366

El-Alaoui, M. (2001). Current disruption during November 24, 1996, substorm. *Journal of Geophysical Research*, *106*(A4), 6229–6245. https://doi.org/10.1029/1999JA000260

El-Alaoui, M., Lapenta, G., Rusaitis, L., & Walker, R. J. (2023a). Plasma sheet turbulence and transport in a coupled fluid-kinetic simulation [global and microscale consequences of mesoscale magnetotail dynamics II]. Retrieved from https://agu.confex.com/agu/fm23/meetingapp.cgi/Paper/1327098

El-Alaoui, M., Richard, R. L., Ashour-Abdalla, M., Goldstein, M. L., & Walker, R. J. (2013). Dipolarization and turbulence in the plasma sheet during a substorm: THEMIS observations and global MHD simulations. *Journal of Geophysical Research: Space Physics*, *118*(12), 7752–7761. https://doi.org/10.1002/2013JA019322

El-Alaoui, M., Walker, R. J., & McPherron, R. L. (2023b). Effects of the ionospheric conductance on the dynamics of the magnetotail. *Journal of Geophysical Research: Space Physics*, *128*(1), e2022JA030259. https://doi.org/10.1029/2022JA030259

El-Alaoui, M., Walker, R. J., Weygand, J. M., Lapenta, G., & Goldstein, M. L. (2021). Magnetohydrodynamic turbulence in the Earth's magnetotail from observations and global MHD simulations. *Frontiers in Astronomy and Space Sciences*, *8*, 16. https://doi.org/10.3389/fspas.2021.620519

Ergun, R. E., Usanova, M. E., Turner, D. L., & Stawarz, J. E. (2022). Bursty bulk flow turbulence as a source of energetic particles to the outer radiation belt. *Geophysical Research Letters*, *49*(11), e2022GL098113. https://doi.org/10.1029/2022GL098113

Frank, L. A. (1967). On the extraterrestrial ring current during geomagnetic storms. *Journal of Geophysical Research*, *72*(15), 3753–3767. https://doi.org/10.1029/JZ072i015p03753

Fuller-Rowell, T., Rees, J. D., Quegan, S., Moffett, R. J., Condrescu, M. V., & Millward, G. H. (1996). A Coupled Thermosphere-Ionosphere Model (CTIM). In *Step: Handbook of ionospheric models*. NOAA/NGDC, Boulder, Colorado: Scientific Committee on Solar Terrestrial Physics (SCOSTEP). 217

Glocer, A., Fok, M., Meng, X., Toth, G., Buzulukova, N., Chen, S., et al. (2013). CRCM + BATS-R-US two-way coupling. *Journal of Geophysical Research: Space Physics*, *118*(4), 1635–1650. https://doi.org/10.1002/jgra.50221

Harel, M., Wolf, R. A., Reiff, P. H., Spiro, R. W., Burke, W. J., Rich, F. J., et al. (1981). Quantitative simulation of a magnetospheric substorm 1. Model logic and overview. *Journal of Geophysical Research*, *86*(A4), 2217–2241. https://doi.org/10.1029/JA086iA04p02217

Jordanova, V. K., Kozyra, J. U., Nagy, A. F., & Khazanov, G. V. (1997). Kinetic model of the ring current-atmosphere interactions. *Journal of Geophysical Research*, *102*(A7), 14279–14291. https://doi.org/10.1029/96JA03699

Kennel, C. F., & Petschek, H. E. (1966). Limit on stably trapped particle fluxes. *Journal of Geophysical Research (1896-1977)*, *71*(1), 1–28. https://doi.org/10.1029/JZ071i001p00001

Lapenta, G. (2017). Exactly energy conserving semi-implicit particle in cell formulation. *Journal of Computational Physics*, *334*, 349–366. https://doi.org/10.1016/j.jcp.2017.01.002

Lapenta, G., Ashour-Abdalla, M., Walker, R. J., & El Alaoui, M. (2016). A multiscale study of ion heating in Earth's magnetotail. *Geophysical Research Letters*, *43*(2), 515–524. https://doi.org/10.1002/2015GL066689

Lapenta, G., El Alaoui, M., Berchem, J., & Walker, R. (2020). Multiscale MHD-kinetic PIC study of energy fluxes caused by reconnection. *Journal of Geophysical Research: Space Physics*, *125*(3), e2019JA027276. https://doi.org/10.1029/2019JA027276

Le, G., Russell, C. T., & Takahashi, K. (2004). Morphology of the ring current derived from magnetic field observations. *Annales Geophysicae*, *22*(4), 1267–1295. https://doi.org/10.5194/angeo-22-1267-2004

Liemohn, M. W., Khazanov, G. V., Craven, P. D., & Kozyra, J. U. (1999). Nonlinear kinetic modeling of early stage plasmaspheric refilling. *Journal of Geophysical Research*, *104*(A5), 10295–10306. https://doi.org/10.1029/1999JA900104

Lin, Y., Wang, X. Y., Lu, S., Perez, J. D., & Lu, Q. (2014). Investigation of storm time magnetotail and ion injection using three-dimensional global hybrid simulation. *Journal of Geophysical Research: Space Physics*, *119*(9), 7413–7432. https://doi.org/10.1002/2014JA020005

Lyon, J., Fedder, J., & Mobarry, C. (2004). The Lyon–Fedder–Mobarry (LFM) global MHD magnetospheric simulation code. *Journal of Atmospheric and Solar-Terrestrial Physics*, *66*(15–16), 1333–1350. https://doi.org/10.1016/j.jastp.2004.03.020

Markidis, S., Lapenta, G., & Rizwan, U. (2010). Multi-scale simulations of plasma with iPIC3D. *Mathematics and Computers in Simulation*, *80*(7), 1509–1519. https://doi.org/10.1016/j.matcom.2009.08.038

McPherron, R. L., El-Alaoui, M., Walker, R. J., Nishimura, Y., & Weygand, J. M. (2020a). The relation of N-S auroral streamers to auroral expansion. *Journal of Geophysical Research: Space Physics*, *125*(4), e2019JA027063. https://doi.org/10.1029/2019JA027063

McPherron, R. L., El-Alaoui, M., Walker, R. J., & Richard, R. (2020b). Characteristics of reconnection sites and fast flow channels in an MHD simulation. *Journal of Geophysical Research: Space Physics*, *125*(9), e2019JA027701. https://doi.org/10.1029/2019JA027701

Merkin, V. G., & Lyon, J. G. (2010). Effects of the low-latitude ionospheric boundary condition on the global magnetosphere. *Journal of Geophysical Research*, *115*(A10), 2010JA015461. https://doi.org/10.1029/2010JA015461

Moen, J., & Brekke, A. (1993). The solar flux influence on quiet time conductances in the auroral ionosphere. *Geophysical Research Letters*, *20*(10), 971–974. https://doi.org/10.1029/92GL02109

Pembroke, A., Toffoletto, F., Sazykin, S., Wiltberger, M., Lyon, J., Merkin, V., et al. (2012). Initial results from a dynamic coupled magnetosphere-ionosphere-ring current model. *Journal of Geophysical Research*, *117*(A2), 2011JA016979. https://doi.org/10.1029/2011JA016979

Raeder, J., Berchem, J., & Ashour-Abdalla, M. (1998). The geospace environment modeling grand challenge: Results from a global geospace circulation model. *Journal of Geophysical Research*, *103*(A7), 14787–14797. https://doi.org/10.1029/98JA00014

Raeder, J., Larson, D., Li, W., Kepko, E. L., & Fuller-Rowell, T. (2008). OpenGGCM simulations for the THEMIS mission. *Space Science Reviews*, *141*(1–4), 535–555. https://doi.org/10.1007/s11214-008-9421-5

Raeder, J., Walker, R. J., & Ashour-Abdalla, M. (1995). The structure of the distant geomagnetic tail during long periods of northward IMF. *Geophysical Research Letters*, *22*(4), 349–352. https://doi.org/10.1029/94GL03380

Richard, L., Khotyaintsev, Y. V., Graham, D. B., Vaivads, A., Gershman, D. J., & Russell, C. T. (2023). Fast ion isotropization by current sheet scattering in magnetic reconnection jets. *Physical Review Letters*, *131*(11), 115201. https://doi.org/10.1103/PhysRevLett.131.115201

Robinson, R. M., Vondrak, R. R., Miller, K., Dabbs, T., & Hardy, D. (1987). On calculating ionospheric conductances from the flux and energy of precipitating electrons. *Journal of Geophysical Research*, *92*(A3), 2565–2569. https://doi.org/10.1029/JA092iA03p02565

Runov, A., Angelopoulos, V., Sitnov, M., Sergeev, V., Nakamura, R., Nishimura, Y., et al. (2011). Dipolarization fronts in the magnetotail plasma sheet. *Planetary and Space Science*, *59*(7), 517–525. https://doi.org/10.1016/j.pss.2010.06.006

Rusaitis, L. (2024a). Dataset for the 2024 ring current paper [Object Object]. *Zenodo*. https://doi.org/10.5281/ZENODO.11040160

Rusaitis, L. (2024b). Rusaitis/2024-Ring-Current-Paper: Zenodo release [Object Object]. *Zenodo*. https://doi.org/10.5281/ZENODO.11039943

Sandhu, J. K., Rae, I. J., Freeman, M. P., Forsyth, C., Gkioulidou, M., Reeves, G. D., et al. (2018). Energization of the ring current by substorms. *Journal of Geophysical Research: Space Physics*, *123*(10), 8131–8148. https://doi.org/10.1029/2018JA025766

Shi, F., Guo, Z., Lin, Y., Wang, X., & Cheng, L. (2023). Magnetotail ion acceleration in 3-D global hybrid simulations. *Journal of Geophysical Research: Space Physics*, *128*(5), e2022JA030980. https://doi.org/10.1029/2022JA030980

Smith, P. H., & Hoffman, R. A. (1973). Ring current particle distributions during the magnetic storms of December 16–18, 1971. *Journal of Geophysical Research*, *78*(22), 4731–4737. https://doi.org/10.1029/JA078i022p04731

Sorathia, K. A., Michael, A., Merkin, V., Ukhorskiy, A., Turner, D. L., Lyon, J., et al. (2021). The role of mesoscale plasma sheet dynamics in ring current formation. *Frontiers in Astronomy and Space Sciences*, *8*, 761875. https://doi.org/10.3389/fspas.2021.761875

Team, T. M. D. (2024). Matplotlib: Visualization with Python [Object Object]. *Zenodo*. https://doi.org/10.5281/ZENODO.10916799

Toffoletto, F., Sazykin, S., Spiro, R., Wolf, R., & Lyon, J. (2004). RCM meets LFM: Initial results of one-way coupling. *Journal of Atmospheric and Solar-Terrestrial Physics*, *66*(15–16), 1361–1370. https://doi.org/10.1016/j.jastp.2004.03.022

Tóth, G., Chen, Y., Gombosi, T. I., Cassak, P., Markidis, S., & Peng, I. B. (2017). Scaling the ion inertial length and its implications for modeling reconnection in global simulations. *Journal of Geophysical Research: Space Physics*, *122*(10), 10336–10355. https://doi.org/10.1002/2017JA024189

Turner, D. L., Cohen, I. J., Michael, A., Sorathia, K., Merkin, S., Mauk, B. H., et al. (2021). Can Earth's magnetotail plasma sheet produce a source of relativistic electrons for the radiation belts? *Geophysical Research Letters*, *48*(21), e2021GL095495. https://doi.org/10.1029/2021GL095495

Walker, R. J., Lapenta, G., Berchem, J., El-Alaoui, M., & Schriver, D. (2019). Embedding particle-in-cell simulations in global magnetohydrodynamic simulations of the magnetosphere. *Journal of Plasma Physics*, *85*(1), 905850109. https://doi.org/10.1017/S0022377819000072

Wang, C.-P., Gkioulidou, M., Lyons, L. R., & Angelopoulos, V. (2012). Spatial distributions of the ion to electron temperature ratio in the magnetosheath and plasma sheet. *Journal of Geophysical Research*, *117*(A8), 2012JA017658. https://doi.org/10.1029/2012JA017658

Williams, D. (1981). Ring current composition and sources: An update. *Planetary and Space Science*, *29*(11), 1195–1203. https://doi.org/10.1016/0032-0633(81)90124-0

Wiltberger, M., Merkin, V., Lyon, J. G., & Ohtani, S. (2015). High-resolution global magnetohydrodynamic simulation of Bursty bulk flows. *Journal of Geophysical Research: Space Physics*, *120*(6), 4555–4566. https://doi.org/10.1002/2015JA021080

Yamada, M., Kulsrud, R., & Ji, H. (2010). Magnetic reconnection. *Reviews of Modern Physics*, *82*(1), 603–664. https://doi.org/10.1103/RevModPhys.82.603

Yang, J., Toffoletto, F. R., Wolf, R. A., & Sazykin, S. (2015). On the contribution of plasma sheet bubbles to the storm time ring current. *Journal of Geophysical Research: Space Physics*, *120*(9), 7416–7432. https://doi.org/10.1002/2015JA021398

Yang, J., Wolf, R., Toffoletto, F., Sazykin, S., Wang, W., & Cui, J. (2019). The inertialized Rice convection model. *Journal of Geophysical Research: Space Physics*, *124*(12), 10294–10317. https://doi.org/10.1029/2019JA026811

Zaharia, S., Jordanova, V. K., Welling, D., & Tóth, G. (2010). Self-consistent inner magnetosphere simulation driven by a global MHD model. *Journal of Geophysical Research*, *115*(A12), 2010JA015915. https://doi.org/10.1029/2010JA015915

Zhang, J., Liemohn, M. W., De Zeeuw, D. L., Borovsky, J. E., Ridley, A. J., Toth, G., et al. (2007). Understanding storm-time ring current development through data-model comparisons of a moderate storm. *Journal of Geophysical Research*, *112*(A4), 2006JA011846. https://doi.org/10.1029/2006JA011846

Zhang, L. Q., Baumjohann, W., Wang, C., Dai, L., & Tang, B. B. (2016). Bursty bulk flows at different magnetospheric activity levels: Dependence on IMF conditions. *Journal of Geophysical Research: Space Physics*, *121*(9), 8773–8789. https://doi.org/10.1002/2016JA022397